Chapter 7: Couplings Between Changes in the Climate System and Biogeochemistry

Coordinating Lead Authors: Guy Brasseur, Kenneth Denman

Lead Authors: Amnat Chidthaisong, Philippe Ciais, Peter Cox, Robert Dickinson, Didier Hauglustaine, Christoph Heinze, Elisabeth Holland, Daniel Jacob, Ulrike Lohmann, Srikanthan Ramachandran, Pedro Leite da Silva Diaz, Steven Wofsy, Xiaoye Zhang

Contributing Authors: David Archer, V. Arora, John Austin, D. Baker, Joe Berry, Gordon Bonan, Philippe Bousquet, Deborah Clark, V. Eyring, Johann Feichter, Pierre Friedlingstein, Inez Fung, Sandro Fuzzi, Sunling Gong, Alex Guenther, Ann Henderson-Sellers, Andy Jones, Bernd Kärcher, Mikio Kawamiya, Yadvinder Malhi, K. Masarie, Surabi Menon, J. Miller, P. Peylin, A. Pitman, Johannes Quaas, P. Rayner, Ulf Riebesell, C. Rödenbeck, Leon Rotstayn, Nigel Roulet, Chris Sabine, Martin Schultz, Michael Schulz, Will Steffen, Steve Schwartz, J. Lee-Taylor, Yuhong Tian, Oliver Wild, Liming Zhou.

Review Editors: Kansri Boonpragob, Martin Heimann, Mario Molina

Date of Draft: 12 August 2005

Notes: This is the TSU compiled version

Figures

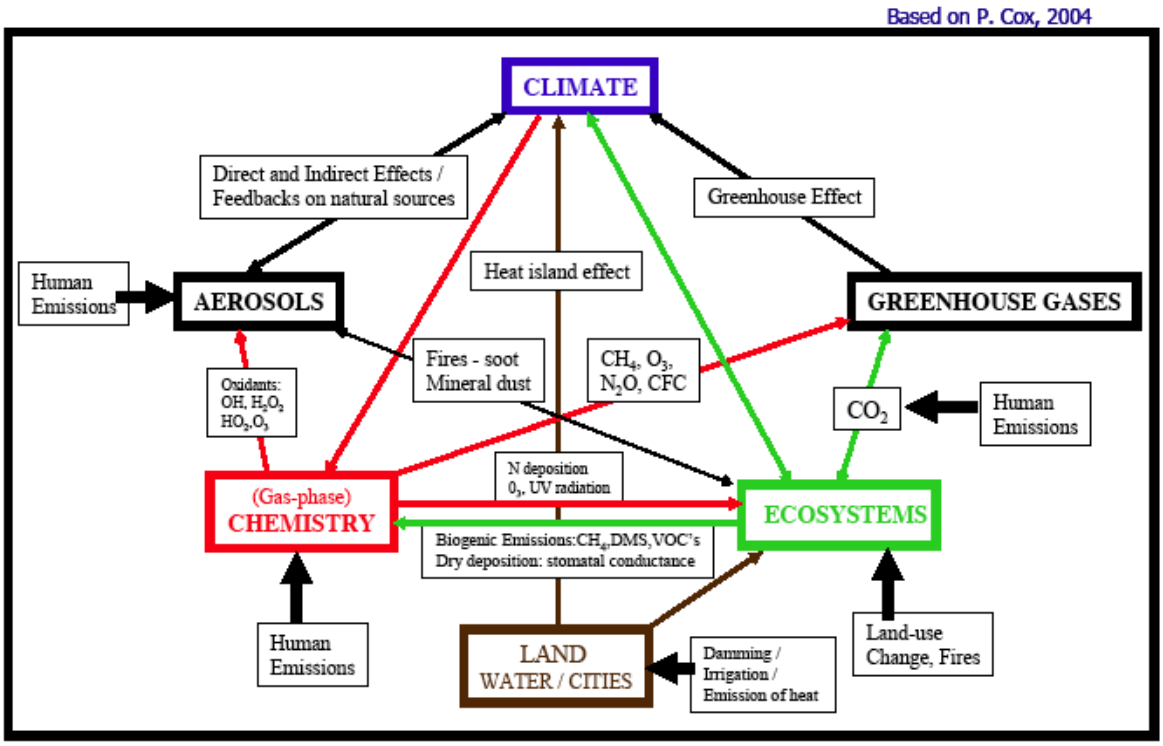

Figure 7.1.1. Schematic representation of some key interactions in the Earth system between climate, greenhouse gases, chemically reactive gases, aerosols and ecosystems. The effects of human activities on different elements of the Earth system are indicated.

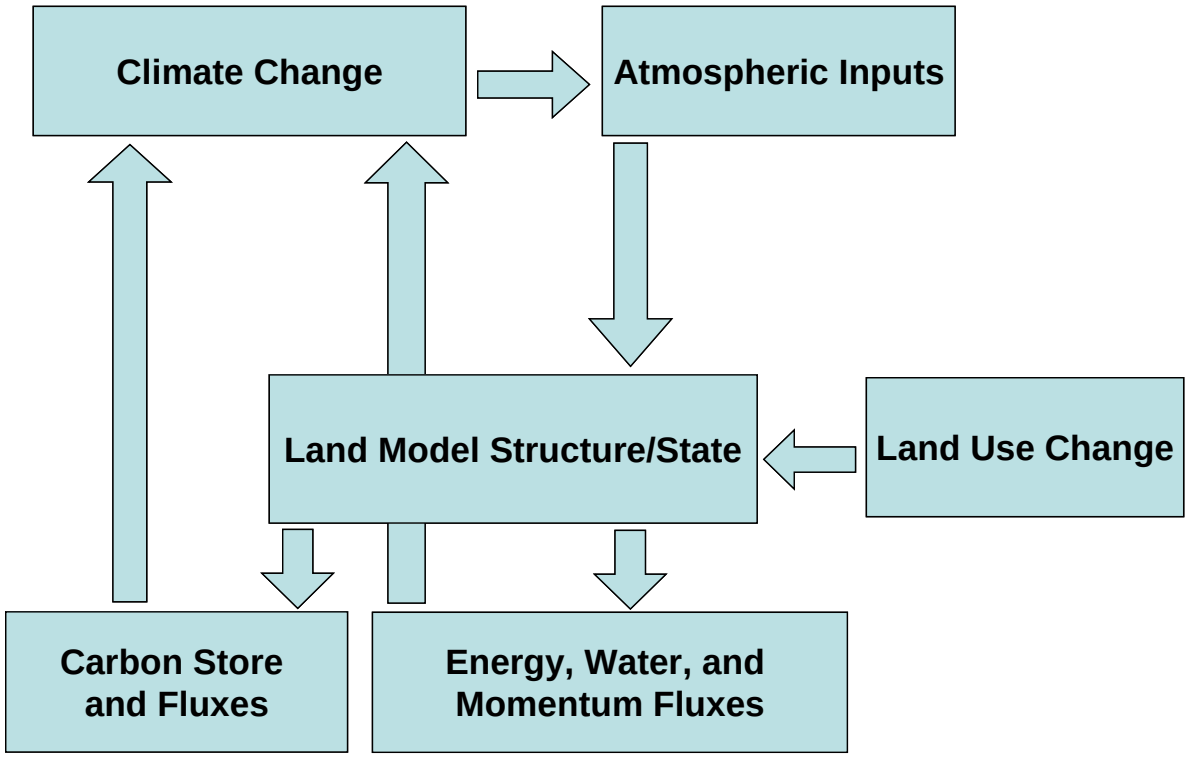

Figure 7.2.1. A schematic depiction of the various factors that must be addressed in evaluating the role of land in anthropogenic climate change.

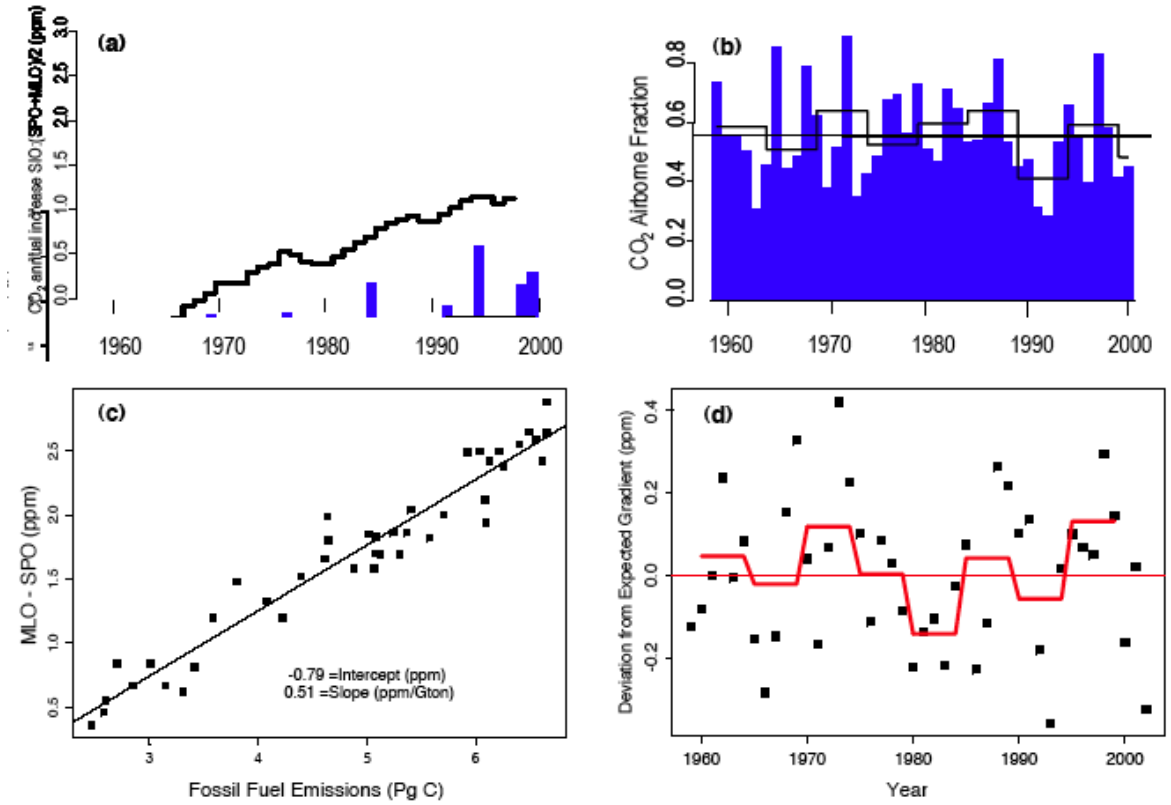

Figure 7.3.1. CO_2 emissions and concentrations in the atmosphere. (a) Annual increases in global CO_2 concentrations as indicated by the mean of Mauna Loa (MLO) and South Pole (SPO) annual averages (***blue bars***), and 5-yr block averages of these data, from Keeling and Whorf (2004; SIO data***, black line***) also shown are data from Conway and Tans (2004, CMDL data, 5-yr block averages (1978–2003), ***red line***). The upper stepped ***bold black line*** shows CO_2 annual increases if 100% of fossil fuel emissions stayed in the atmosphere. (b) Fraction of fossil fuel emissions remaining in the atmosphere each year ("Airborne fraction", ***blue bars***), 5-yr mean (***stepped line*** –) (SIO data), and mean since 1958 (***broken line*** ---). Note the anomalously low airborne fraction in the early 1990s. (c) North-south concentration difference, as indicated by MLO — SPO (ppm) , plotted against annual fossil fuel emission flux (Pg-C), 1959–2003. (d) Deviation of the annual mean concentration different (MLO – SPO) from the line in panel (c), with 5-yr block averages in **red —**.

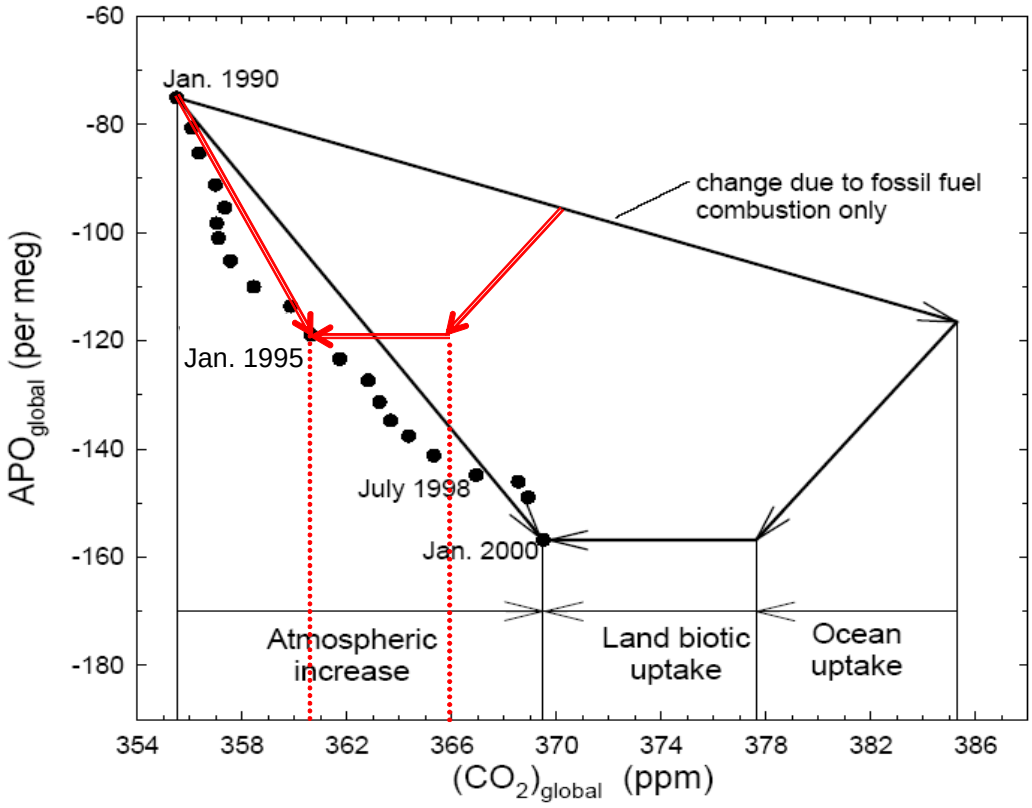

Figure 7.3.2. Semi-annual changes in Atmospheric Potential Oxygen (APO): $\Delta APO = \Delta O_2 + \alpha_B \Delta CO_2$, where α_B represents the average O_2:CO_2 molar exchange ratio (≅1.10) for land biotic photosynthesis and respiration and ΔO_2 and ΔCO_2 are defined from global data for the O_2:N_2 ratio and for CO_2 mole fraction, respectively. APO is defined so that uptake or release by land biota has no effect. Fossil fuel inputs lower APO (slope ($\alpha_B - \alpha_\Phi$ due to the higher value of α_Φ (≅1.4). Dissolution of CO_2 in the ocean has slope α_B since O_2 is not taken up. The analysis corrected for ΔO_2 associated with outgassing of O_2 associated with warming of the upper ocean. From Manning and Keeling (2005).

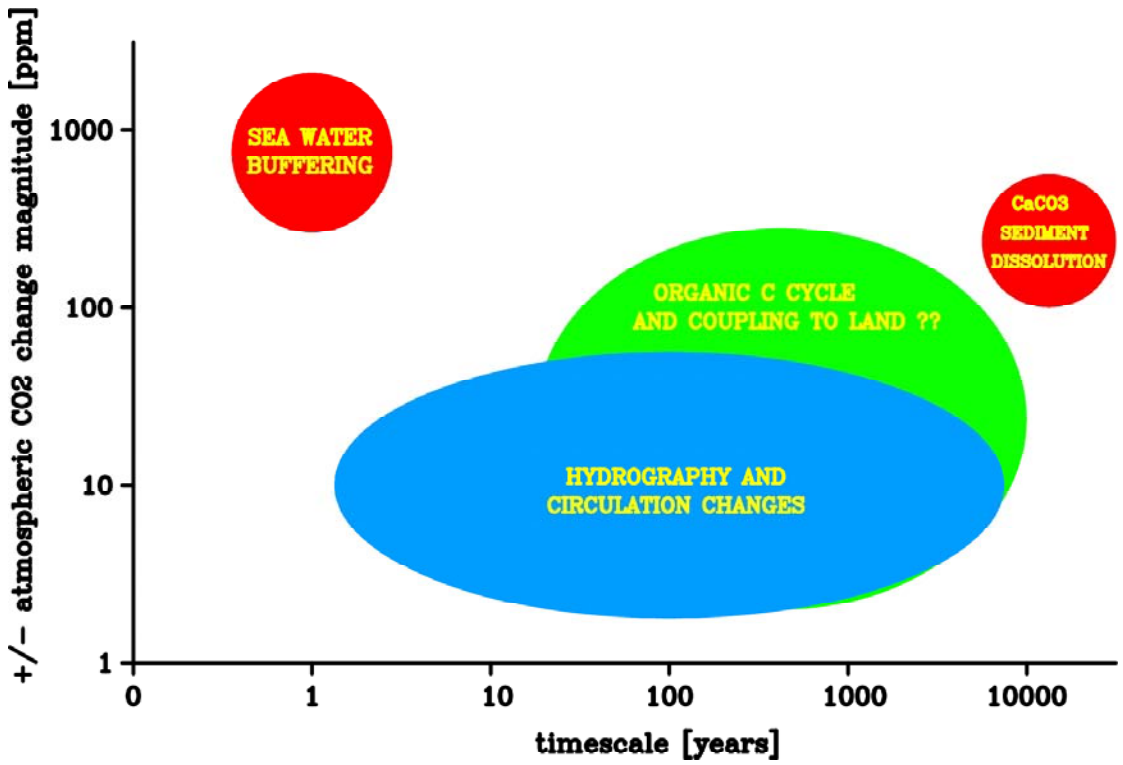

Figure 7.3.3. Overview of biogeochemical ocean climate feedbacks (see also Table 7.3.2.2.1).

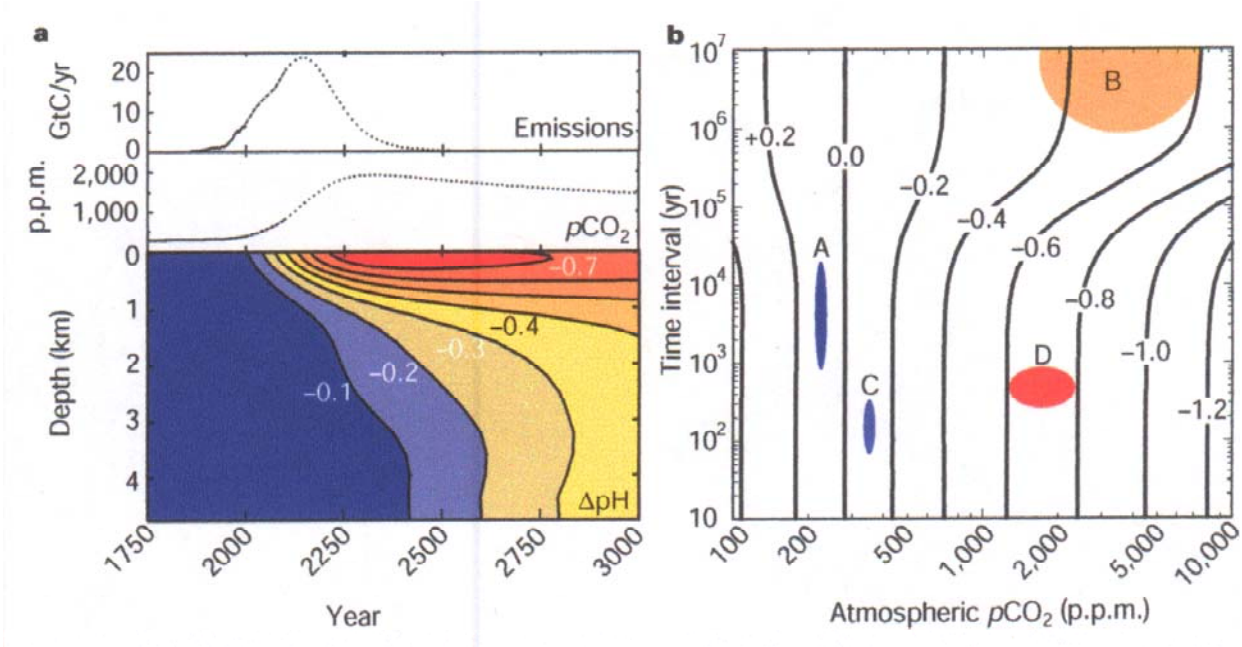

Figure 7.3.4. Atmospheric release of CO_2 from the burning of fossil fuels may give rise to a marked increase in ocean acidity. (a, left) Atmospheric CO_2 emissions, historical atmospheric CO_2 levels and predicted CO_2 concentrations from this emissions scenario, together with changes in ocean *p*H based on horizontally averaged chemistry. (b, right) Estimated maximum change in surface ocean *p*H as a function of final atmospheric CO_2 pressure, and the transition time over which this CO_2 pressure is linearly approached from 280 μatm. A. Glacial-interglacial changes; B. slow changes over the past 300 Myr; C. historical changes in ocean surface waters; D. unabated fossil-fuel burning over the next few centuries. Figure and caption from Caldeira and Wickett (2003).

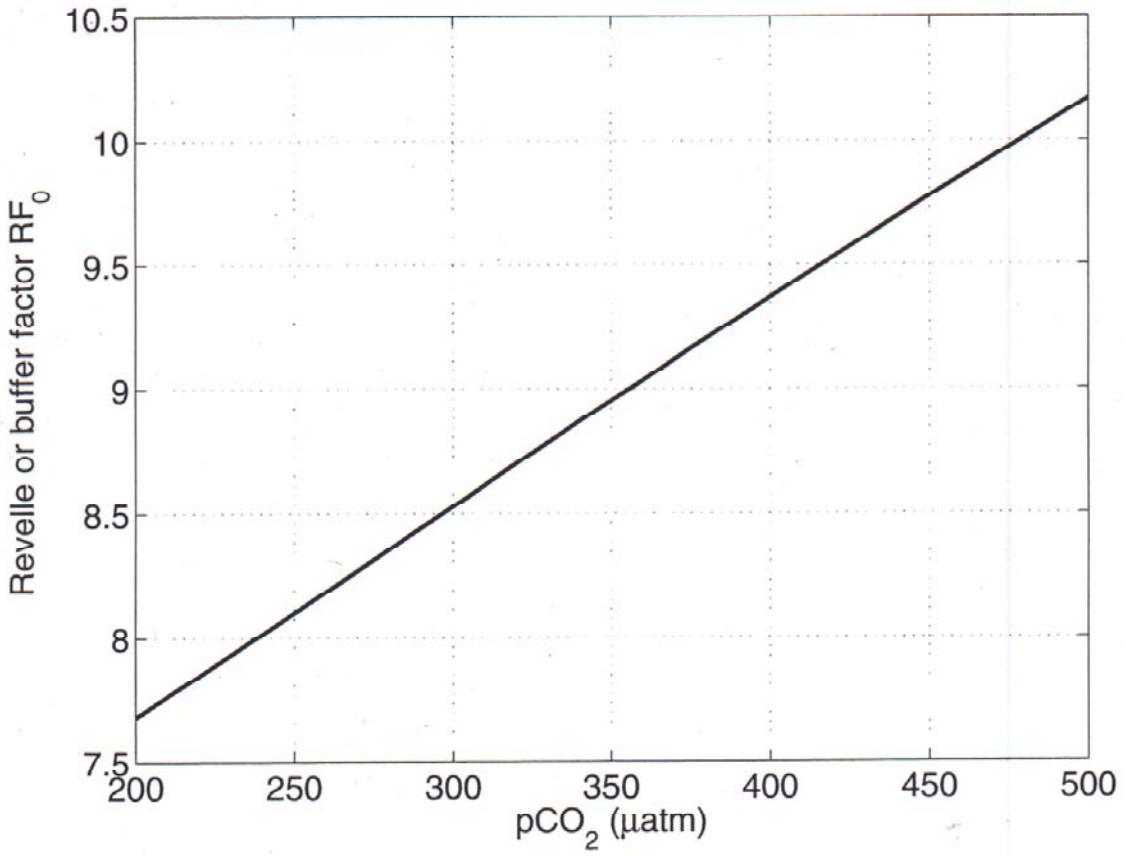

Figure 7.3.5. The Revelle factor RF_0 as a function of pCO_2 (T_C = 25º, S = 35, TA = 2300 µmol kg^{-1}). With increasing partial pressure of CO_2 the Revelle factor increases and thus the buffering capacity of the ocean decreases. Figure and caption from Zeebe and Wolf-Gladrow (2001).

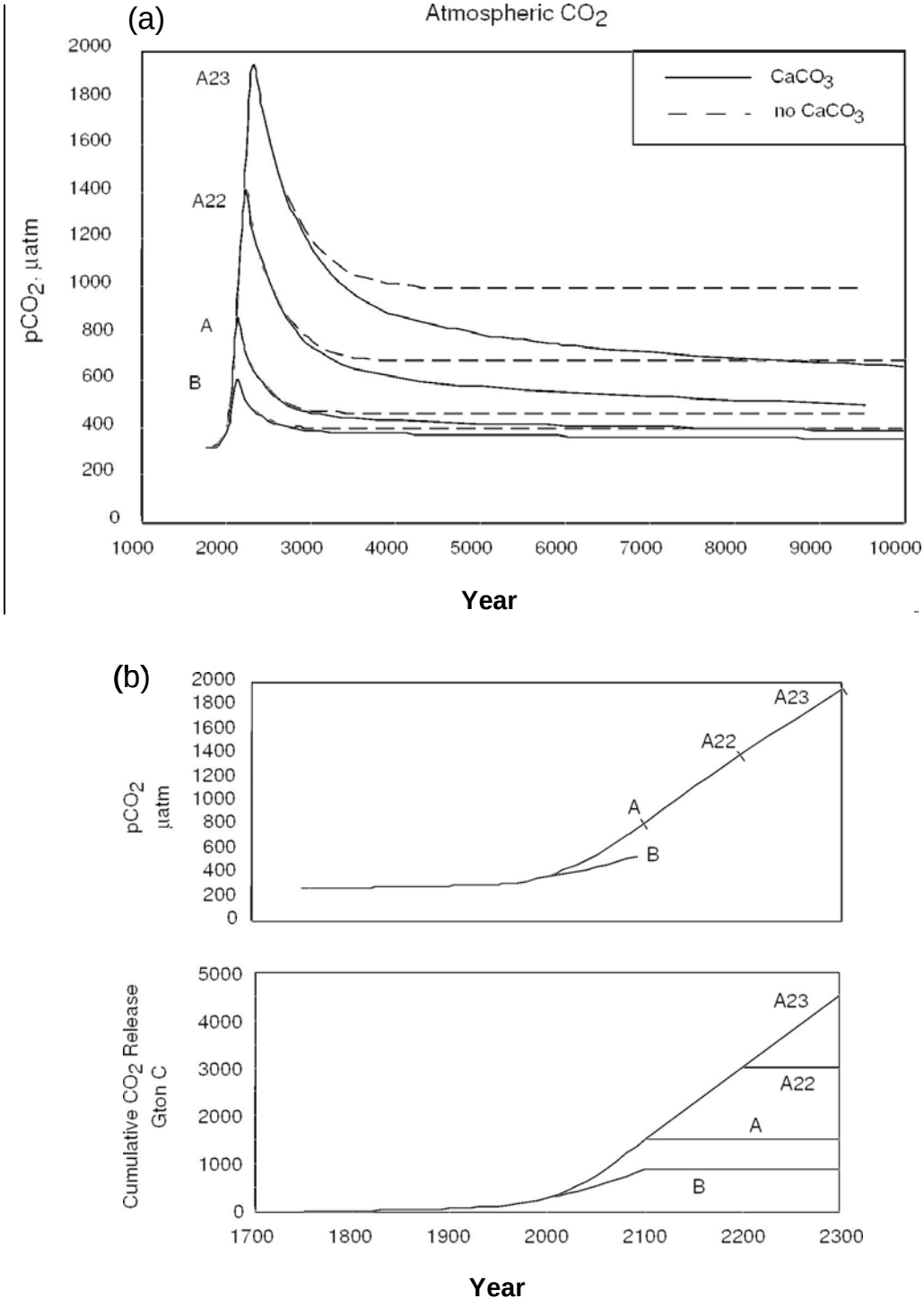

Figure 7.3.6. Panel a: Model response to anthropogenic CO_2 release to the year AD 10,000, including the effect of $CaCO_3$ dissolution from sediments (solid curve), and neglecting $CaCO_3$ (dashed curve). The pCO_2 is held to IPCC projections for scenarios A and B to the year 2100 and extrapolated to the years 2200 and 2300 at the scenario A year 2100 emission rate for runs B, A, A22, and A23 respectively. After those times, a zero net terrestrial release of CO_2 is specified. Panel b: Emission scenarios used. (From Archer et al., 1998)

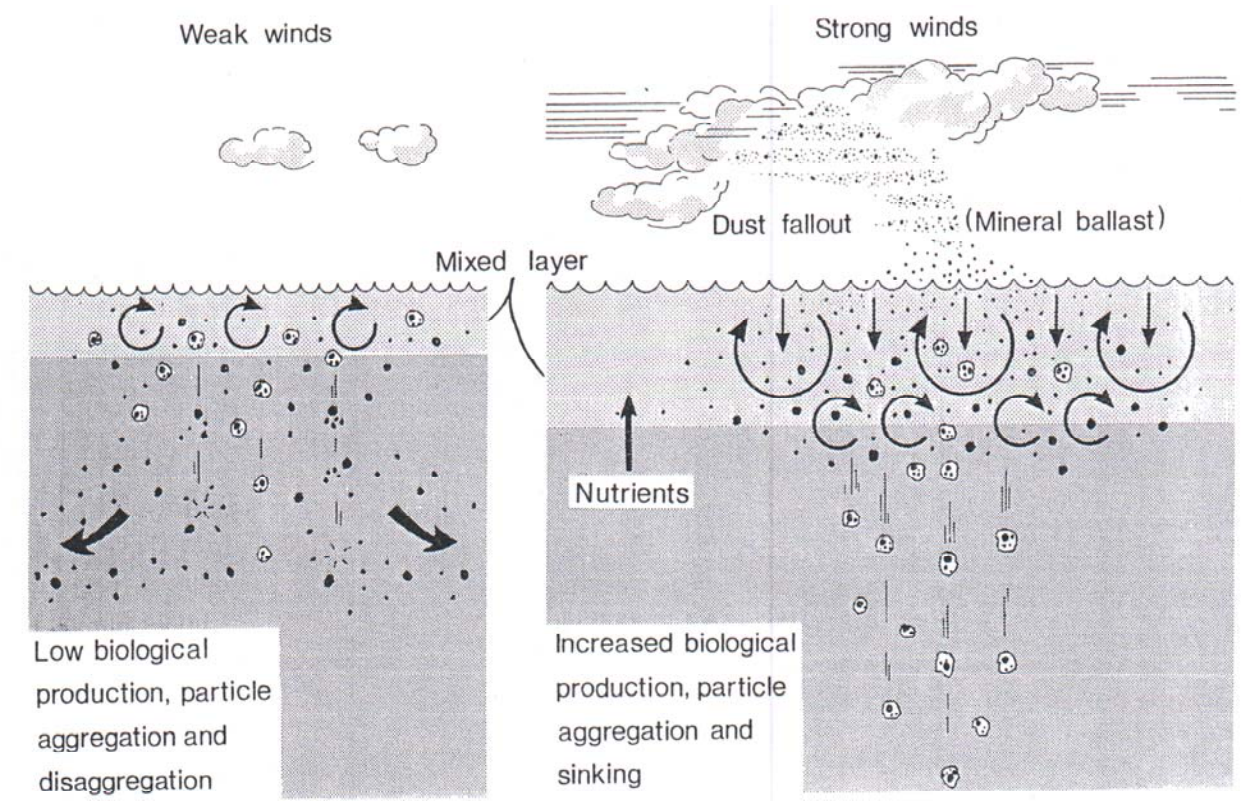

Figure 7.3.7. The wind-driven biological pump and its enhancement by atmospheric dust deposition over the sea. Figure and caption from Ittekkot (1993).

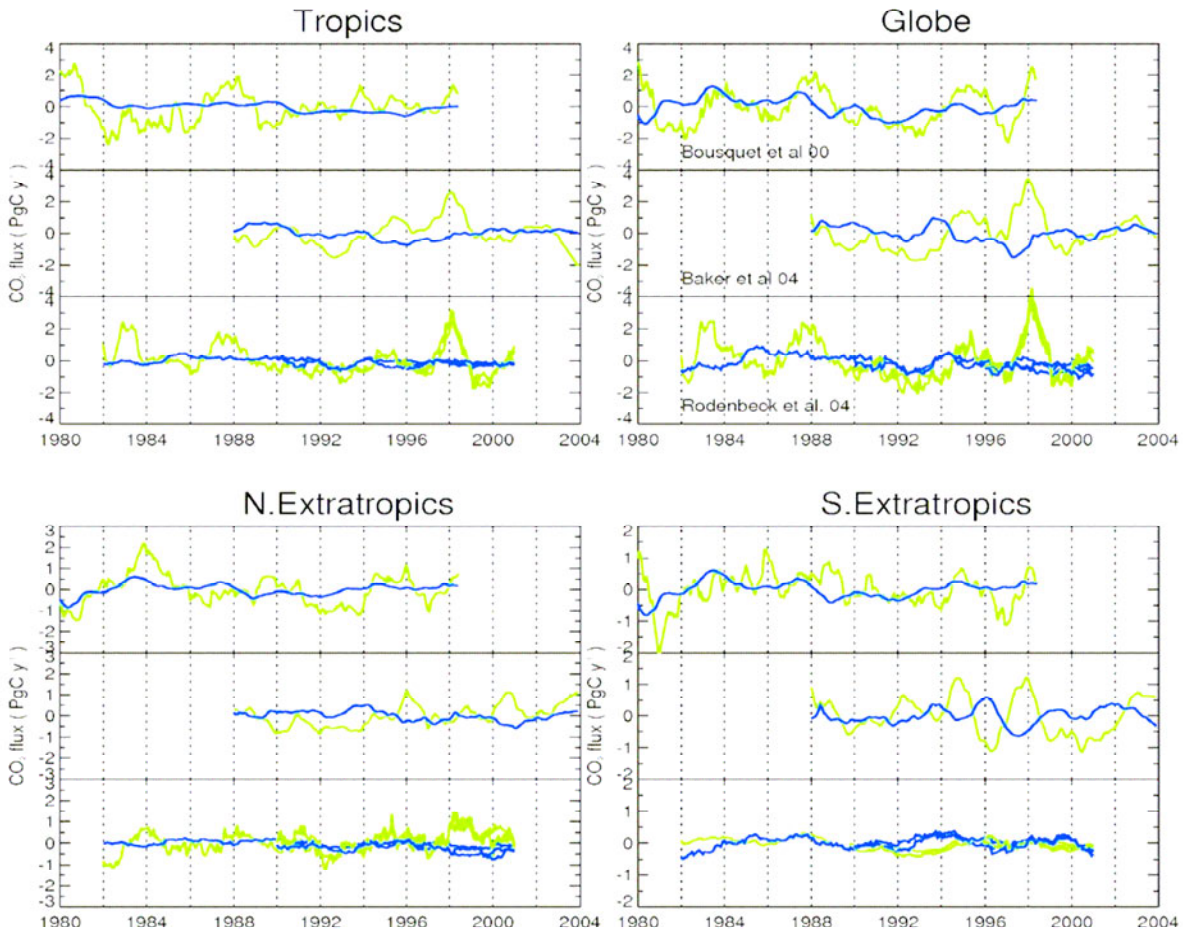

Figure 7.3.8. Ocean and land fluxes year-to-year variations from inversions summed into large latitude bands, and over the globe during approx. the past 20 years. Three different inversion ensembles are shown, and for each flux and each region, the long term mean values has been substracted and the seasonal signal has been removed.

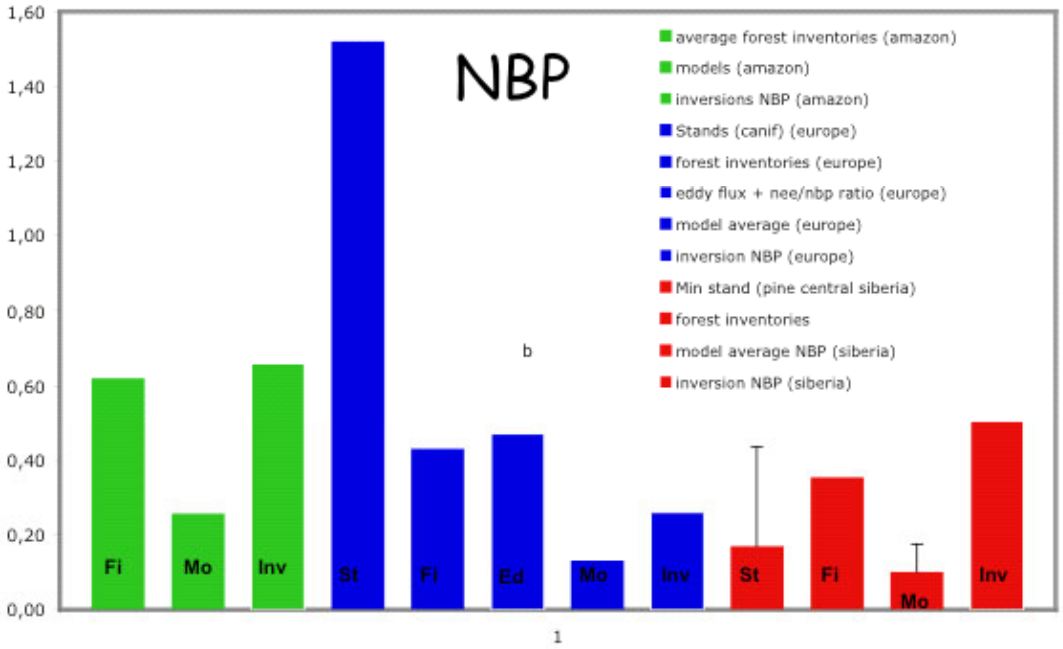

Figure 7.3.9. Estimates of the mean terrestrial carbon balance (in tC per ha per year) from different approaches at various scales and for three distinct biomes, **Green** = Amazon ; **Blue** = Western Europe ; **Red** = Siberia (data compiled by Ciais et al., 2005).

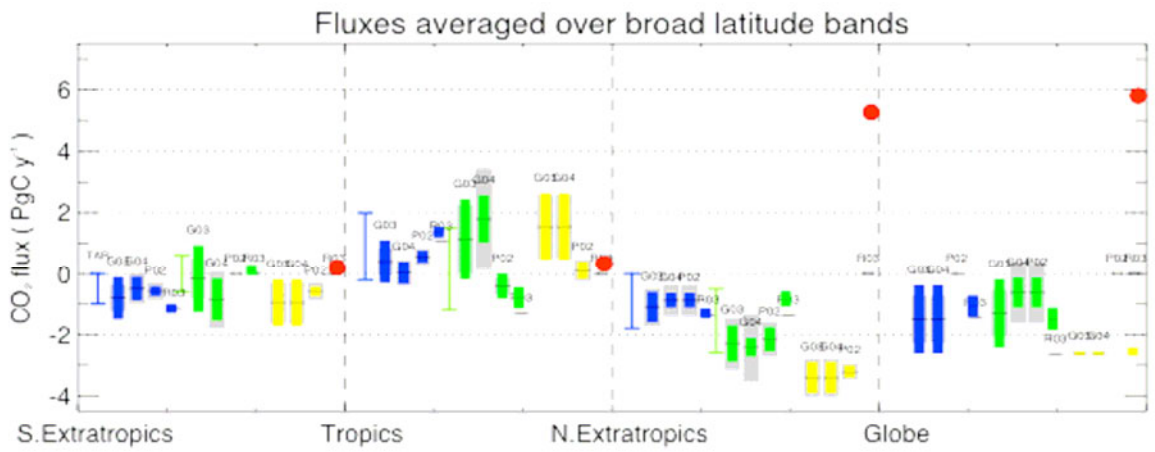

Figure 7.3.10. Ocean and land fluxes from inversions summed into large latitude bands, and over the globe during the period 1992–1996. **Blue** = Ocean fluxes, **Green** = land fluxes, **Yellow** = total land plus ocean fluxes obtained after subtracting the non-optimized fossil fuel emissions in **red**. The mean flux from different ensembles of inversions is reported together with random errrors and the range of bias due to different settings within each ensemble. Error boxes in colour are the average of 1-s Gaussian random errors returned by each member of the ensemble. Grey error boxes are the spread of the mean fluxes from different arbitrary settings. **TAR** = range of mean fluxes from Third Assessment Report ; **G02** = ensemble using annual mean CO_2 observations with grey error from 16 transport models (Gurney et al., 2002); **G03** is the ensemble using smoothed monthly CO_2 observations with grey error from 13 transport models (also from Gurney et al., 2003) ; **P04** is the ensemble with grey error from 3 transport models times 3 grouping of large regions times 3 inversion set of regions (Peylin et al., 2005a); **R03** is the ensemble where the fluxes are solved for many small regions using monthly flask data, with the grey error from different sensitivity inversions (Rodenbeck et al., 2003).

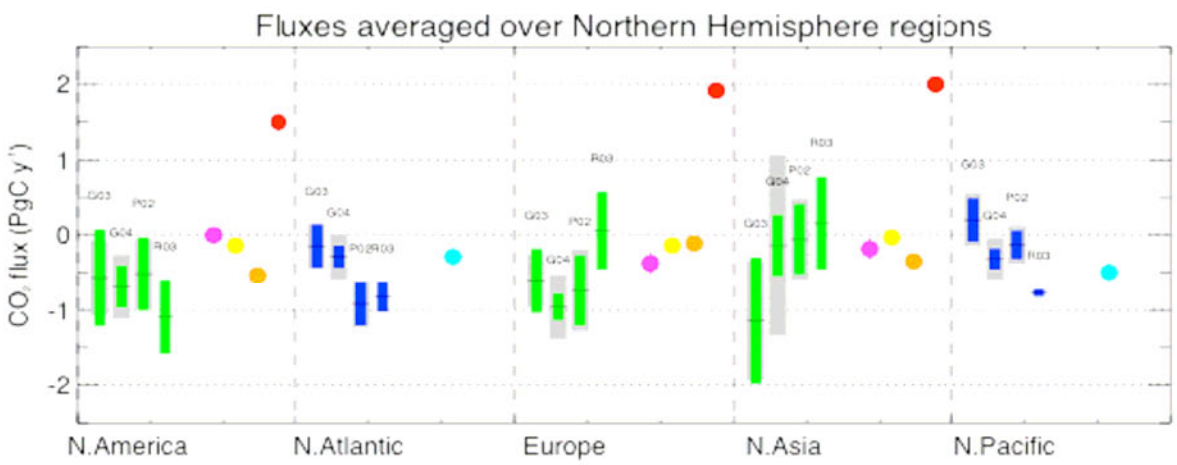

Figure 7.3.11. Blue, Green = Ocean and land fluxes from inversions in the Northern Hemisphere. Bottom-up continental-wide or ocean-basin-wide estimates are given separately. **Magenta** = Forest biomass inventory data for Europe (Nabuurs et al., 1997) and Siberia (Shvidenko and Nilsson, 2003); **Yellow** = Forest biomass inventory data including Russia, Mongolia and China (Goodale et al., 2002); **Orange** = bottom-up synthesis of the net carbon balance of coterminous U.S. (Pacala et al., 2001), Geographic Europe (Janssens et al., 2003), and Russia (Shvidenko and Nilsson, 2003). **Cyan** = air-sea basin scale fluxes (Takahashi et al., 1999).

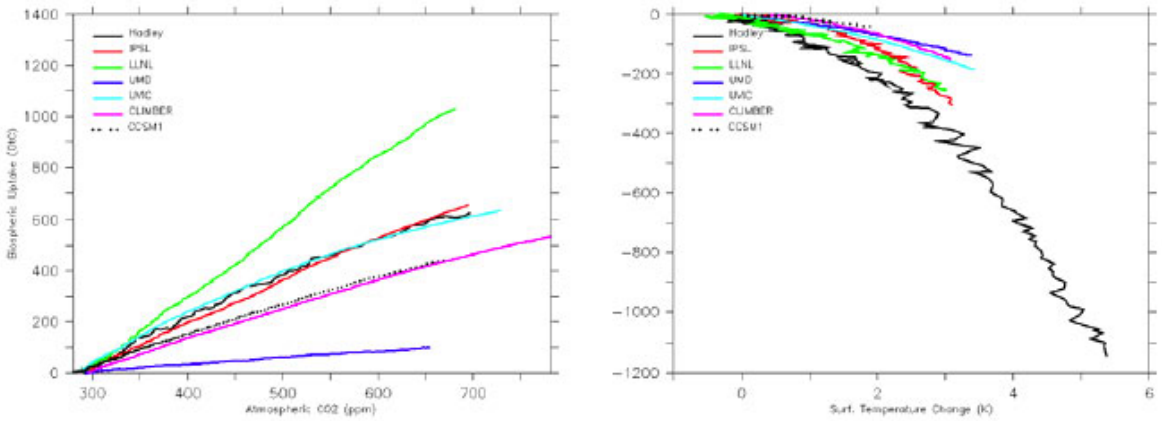

Figure 7.3.12. (a) Change in land carbon storage (Pg-C) versus atmospheric CO_2 concentration (ppm) for the C^4MIP uncoupled simulations. The mean gradient of each line is the parameter β_L. (b) Change in land carbon storage (Pg-C) with global warming (K). In this case the mean gradient of each line is the parameter γ_L. (c) Like (a), but for β_O. (d) Like (b), but for γ_O.

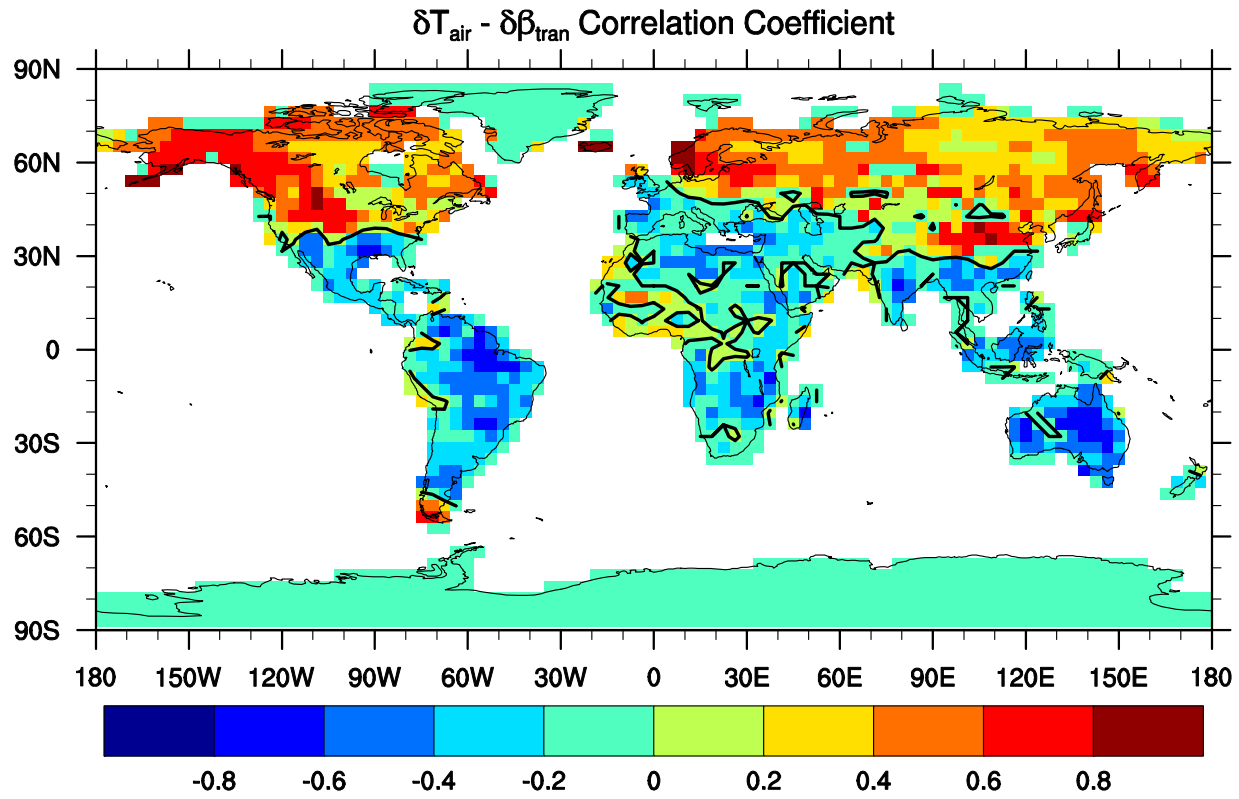

Figure 7.3.13. Correlations between temperature and soil moisture changes between the coupled and uncoupled runs from the NCAR-CSM1 model, showing the tendency towards warmer-drier conditions in the tropics and warmer-moister conditions at high latitudes (from Fung et al., 2005).

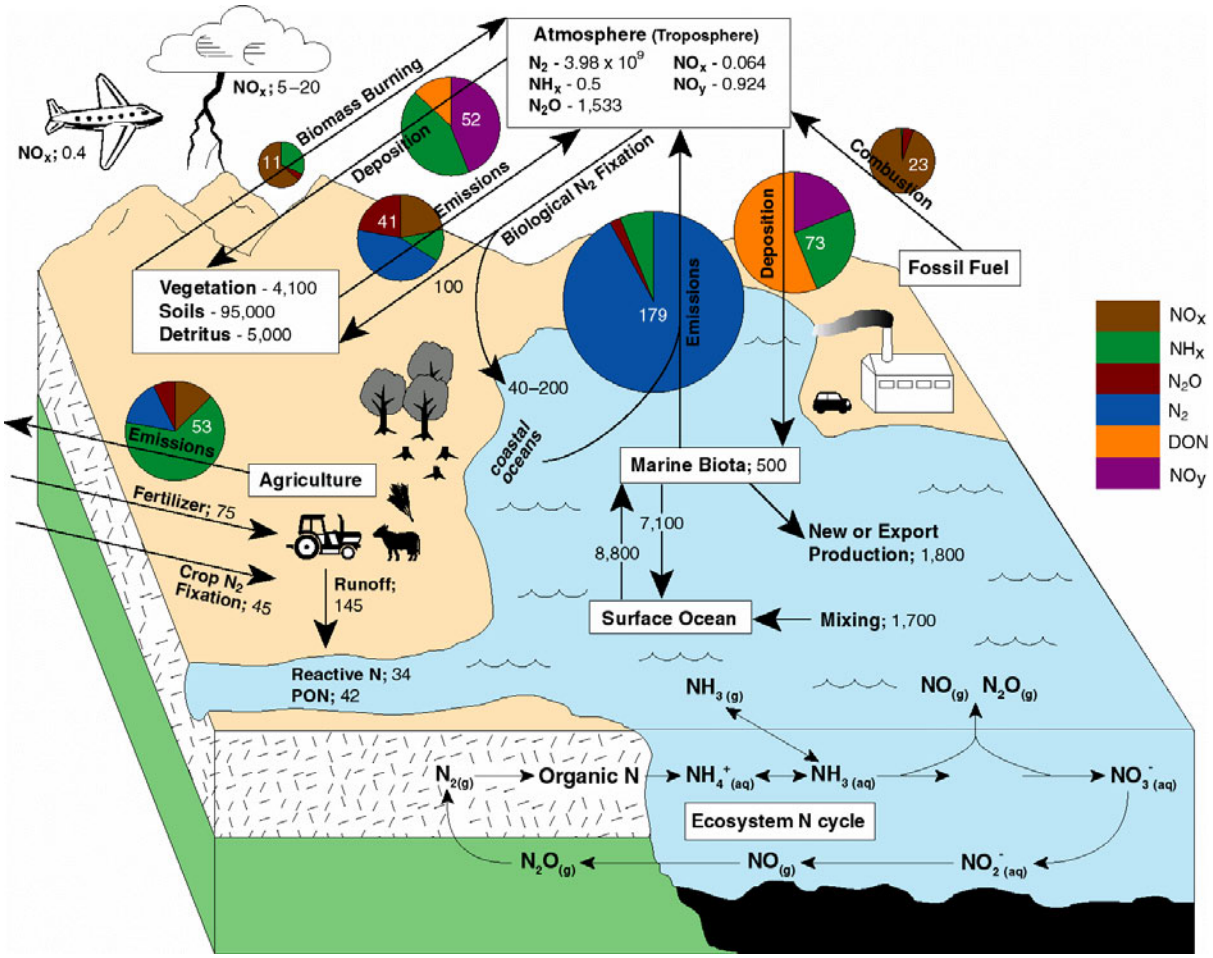

Figure 7.4.1. Key fluxes and components of the global nitrogen cycle, including emissions and deposition. Each of the key atmospheric species including NO_x ($NO + NO_2$), NH_x($NH_3 + NH_4^+$), N_2O, N_2, DON (Dissolved Organic Nitrogen) and NOy (total odd nitrogen= $NO_x + HNO_3 + HONO + HO_2NO_2 + NO_3$ + nitrate radical + Peroxyacetyl nitrates + N_2O_5 + organic nitrates) and their fluxes are shown. The ecosystem nitrogen cycle depicts the internal transformations nitrogen going starting with N_2, and the transformation, nitrification and denitrification, back to N_2 to complete the full cycle. All units are in Tg of N, Tg= 10^{12} g.

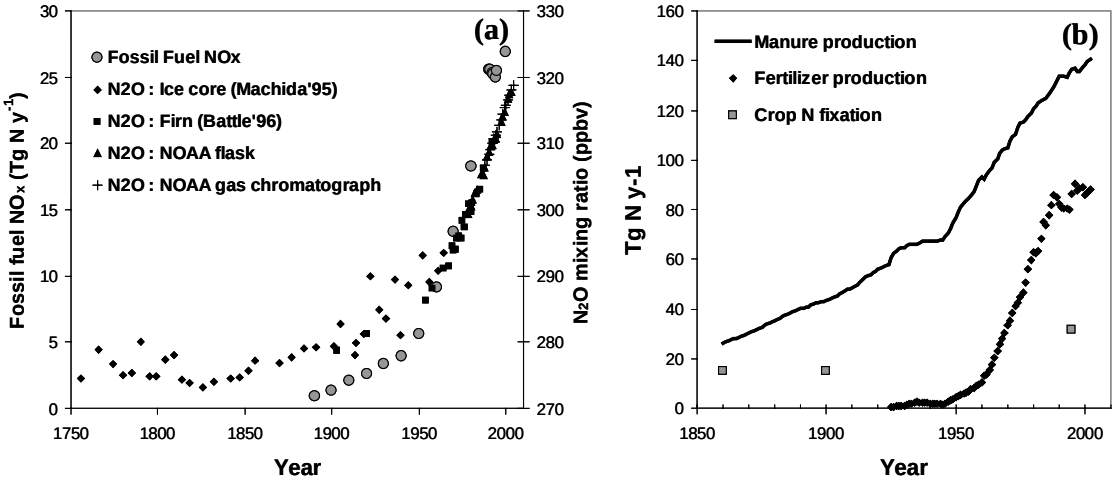

Figure 7.4.2. (a) Changes in the emissions of fossil fuel NO_x and atmospheric N_2O mixing ratios since 1750. N_2O mixing ratios provide the atmospheric measurement constraint on global changes to the nitrogen cycle. (b) Changes in the indices of global agricultural nitrogen cycle since 1850: the production of manure, fertilizer and estimates of crop nitrogen fixation. For data sources see http://www-eosdis.ornl.gov/ and http://www.cmdl.noaa.gov/.

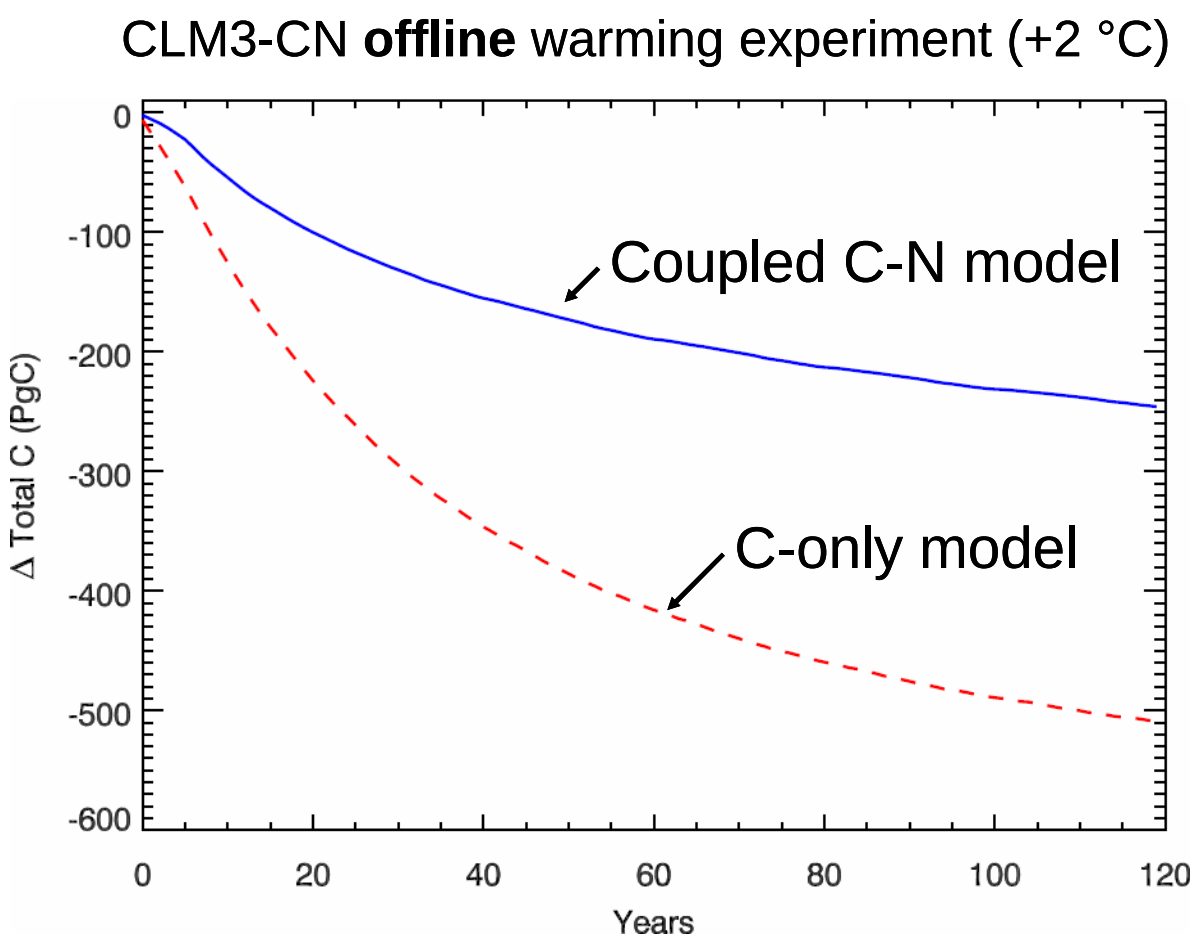

Figure 7.4.3. Simulated net global terrestrial carbon release using a carbon model and a coupled carbon nitrogen model. The simulations were done using the Community Land Model (Bonan version 3.0 modified to include carbon and carbon and nitrogen. The simulation was a step function 2°C increase in temperature forcing of the model applied after a spin-up of the carbon or carbon nitrogen model.

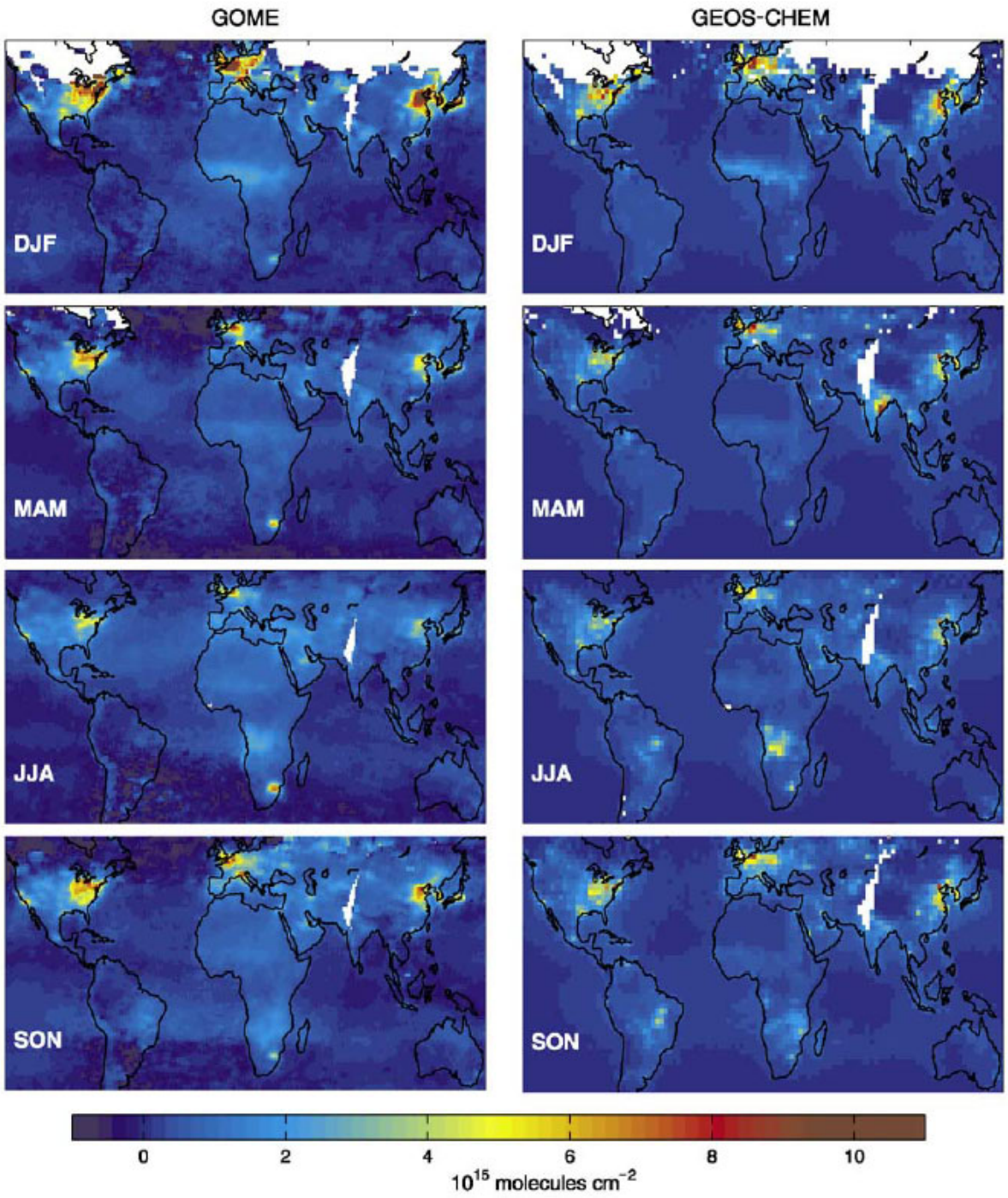

Figure 7.4.4. Seasonal mean tropospheric NO_2 columns for September 1996–August 1997. Left: GOME retrievals. Right: GEOS-CHEM model simulation sampled along GOME overpasses and using sources from Table 7.4.6 (Bey et al., 2001). White areas have no GOME data. From Martin et al. (2003b)

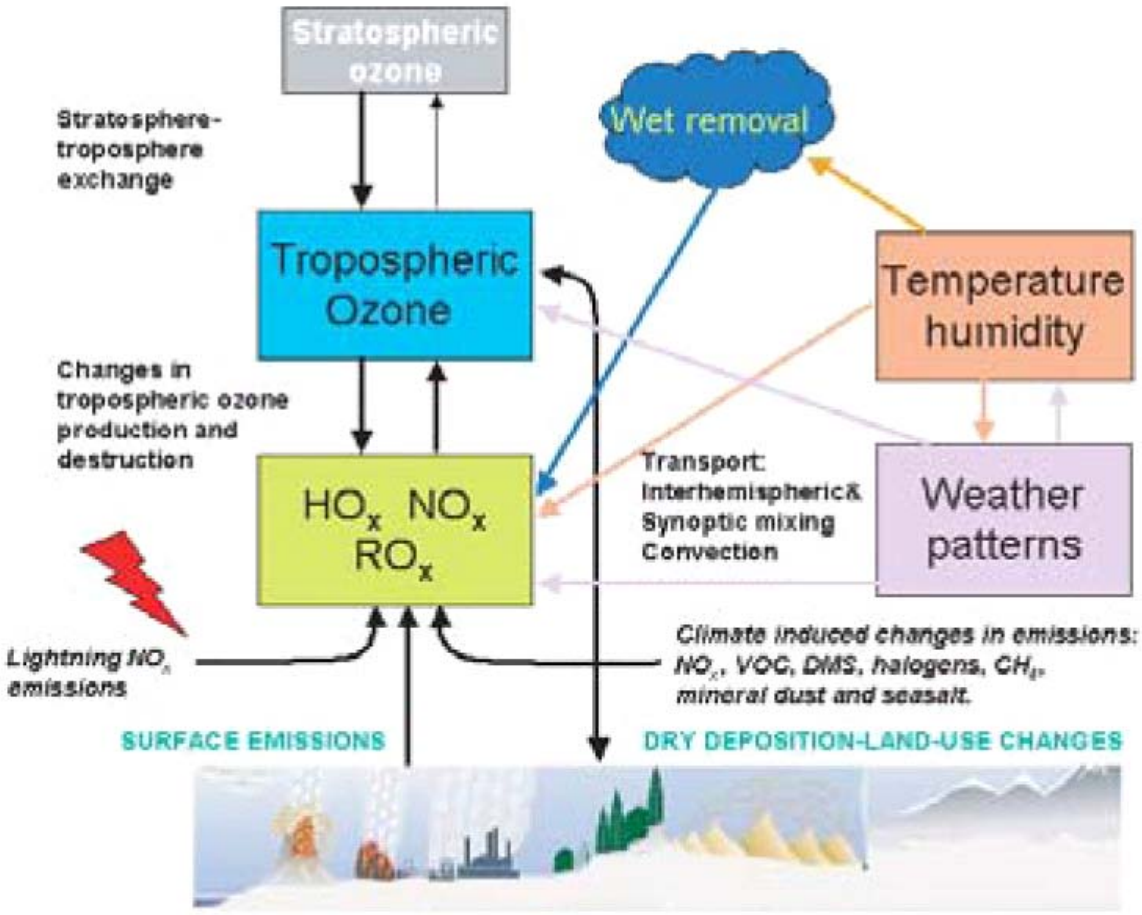

Figure 7.4.5. Climate variables affecting tropospheric ozone. From European Commission (2003).

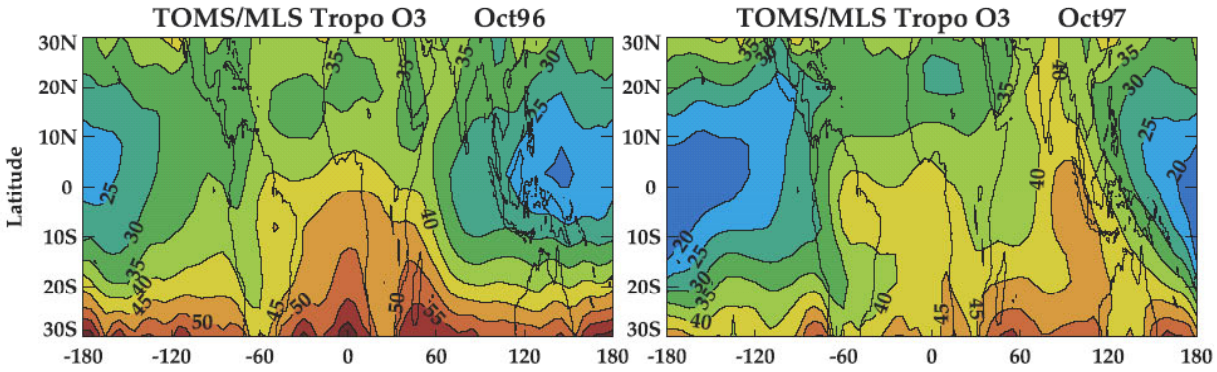

Figure 7.4.6. ENSO effect on tropospheric ozone columns as observed from TOMS/MLS. Monthly mean columns (DU) are shown for October 1996 (cold phase) and October 1997 (warm phase). From Chandra et al. (2003).

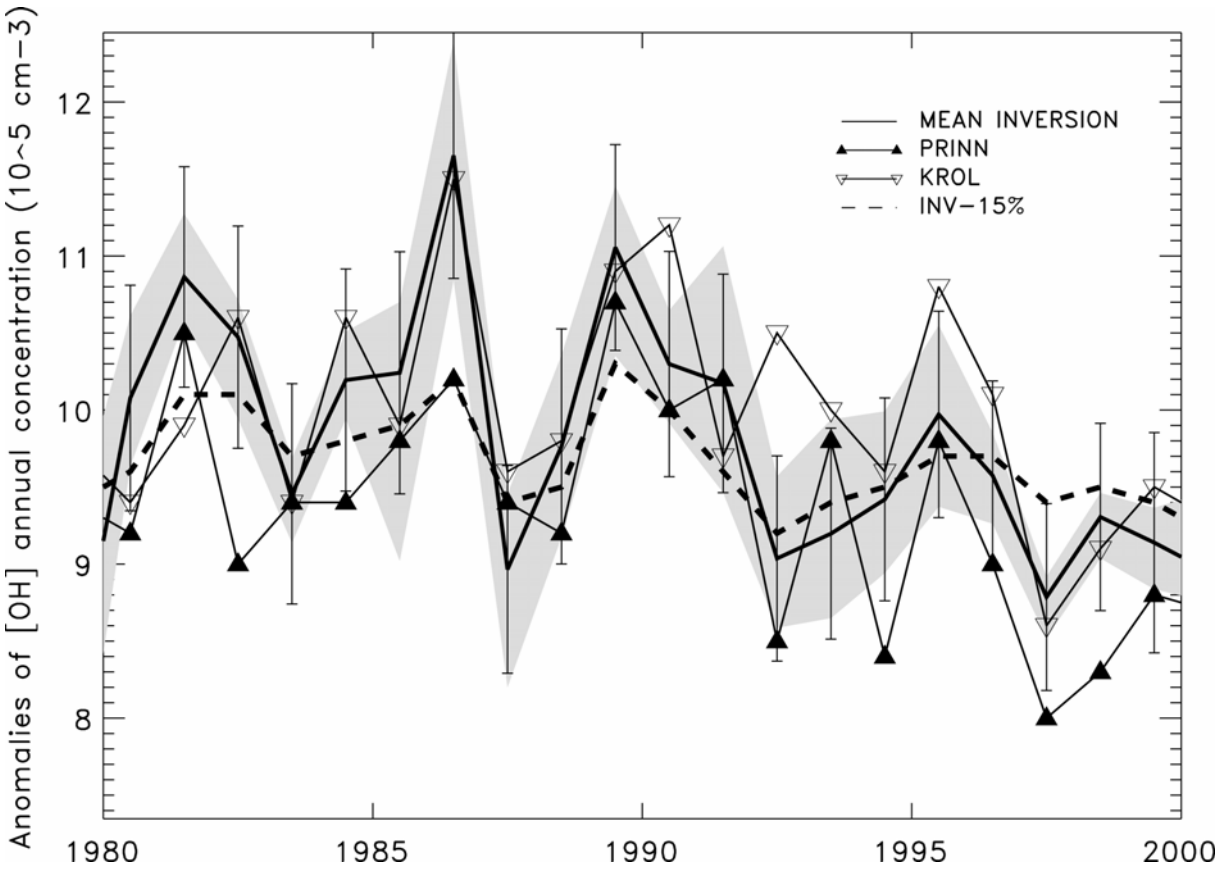

Figure 7.4.7. Annual and global mean OH variations calculated by Bousquet et al. (2005) as the mean of a set of inversions of CH_3CCl_3 observations from ALE/GAGE/AGAGE network. Loose prior OH uncertainties are applied in all 16 inversions (±100%). The mean inversion (solid line) is compared with estimates from Prinn et al. (2001) (open triangles) and from Krol et al. (2003) (filled triangles). The shaded area denotes the envelope of all inversions. Dashed line is the results of an inversion in which OH prior error is tighter (±15%) but still gives CH_3CCl_3 sources that are compatible with the inventory of McCulloch and Midgley (2001) at ±2σ level.

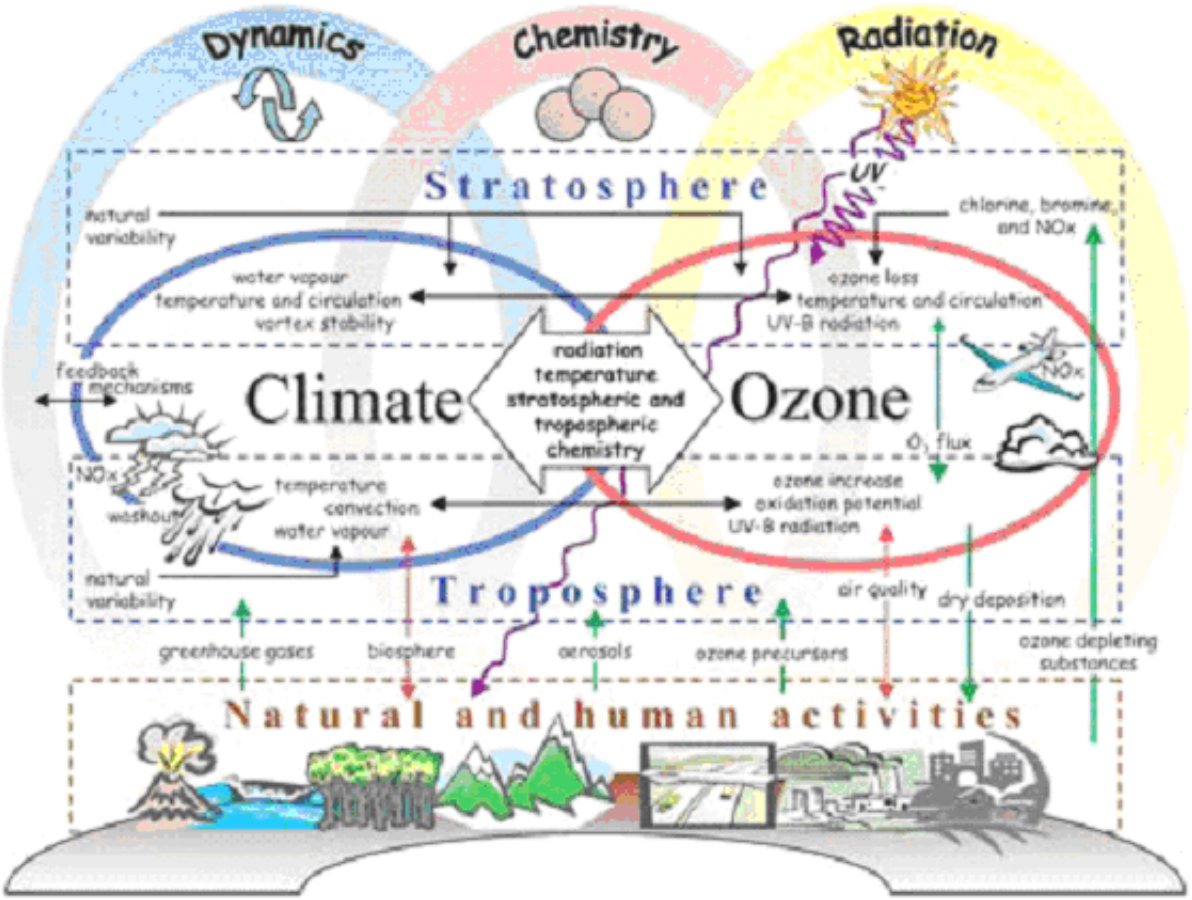

Figure 7.4.8. Processes determining the ozone climate interactions in the troposphere and the stratosphere (European Commission, 2003). Atmospheric regions are indicated by blue, and source regions by brown dashed boxes.

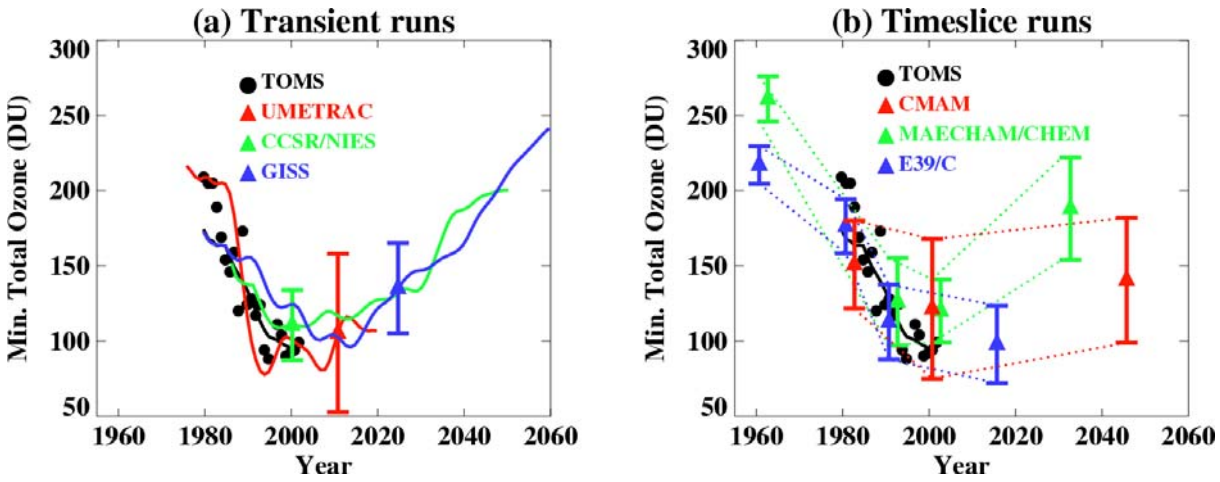

Figure 7.4.9. Minimum Antarctic (September to November) total ozone evolution for (a) transient runs and (b) time slice runs of different CCM model experiments in comparison with TOMS data for the period 1960 to 2060. The solid lines in (a) show the results of a Gaussian smoother applied to the individual year's results. The error bars denote twice the standard deviation of the individual years from the smoothed curve. For the time slice experiments the dotted lines are drawn between the end points of the error bars to assist in estimating trends (Austin et al., 2003; their Figure 10).

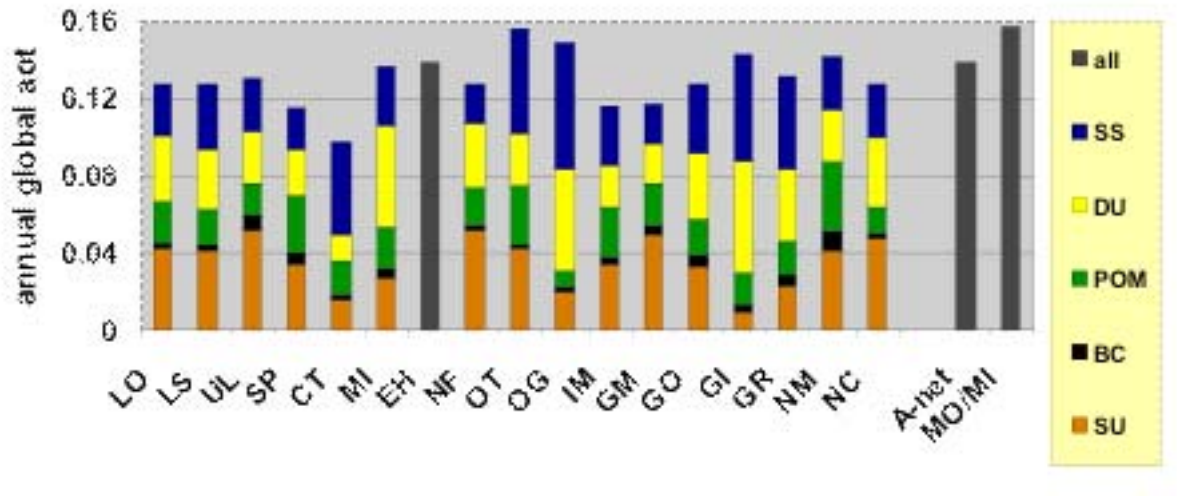

Figure 7.5.1. Individual contributions of the five aerosol components (SS-seasalt, DU-dust, POM-particulate organic matter, BC-black carbon, SU-sulphate) to the annual global aerosol optical thickness (at 550nm) from different global models. For comparison, two aot data references from remote sensing are provided: AERONET and a satellite-composite of MODIS (ocean) and MISR (land) data. Adapted from Kinne et al. (2005).

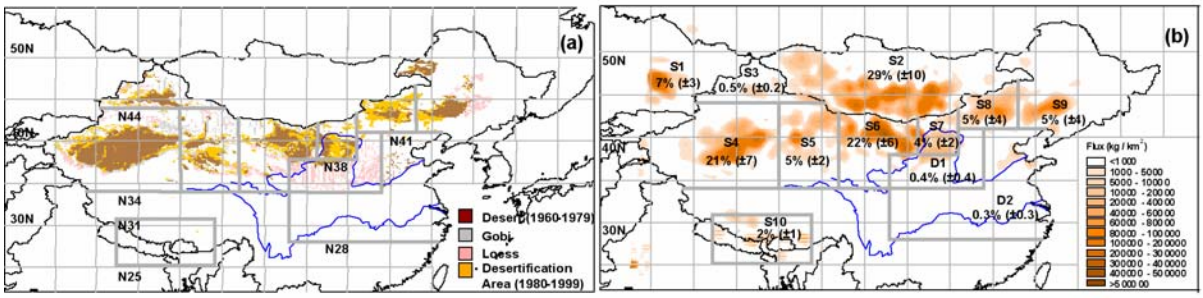

Figure 7.5.2. (a) Chinese desert distributions from 1960–1979 and desert plus desertification areas from 1980–1999; (b) Sources (S1 to S10) and typical depositional areas (D1 and D2) for Asian dust indicated by spring average dust emission flux (kg km^{-2} months^{-1}) between 1960–2002. The percentages with standard deviation in the parenthesis denote the average amount of dust production in each source region and the total amount of emissions between 1960–2002. The deserts in Mongolia (S2) and in western (S4) and northern (S6) China (mainly the Taklimakan and Badain Juran, respectively) can be considered as the major sources for Asian dust emissions. Several areas with more expansions of deserts (S7, S8, S9 and S5) are not key sources. Adapted from Zhang et al., (2003).

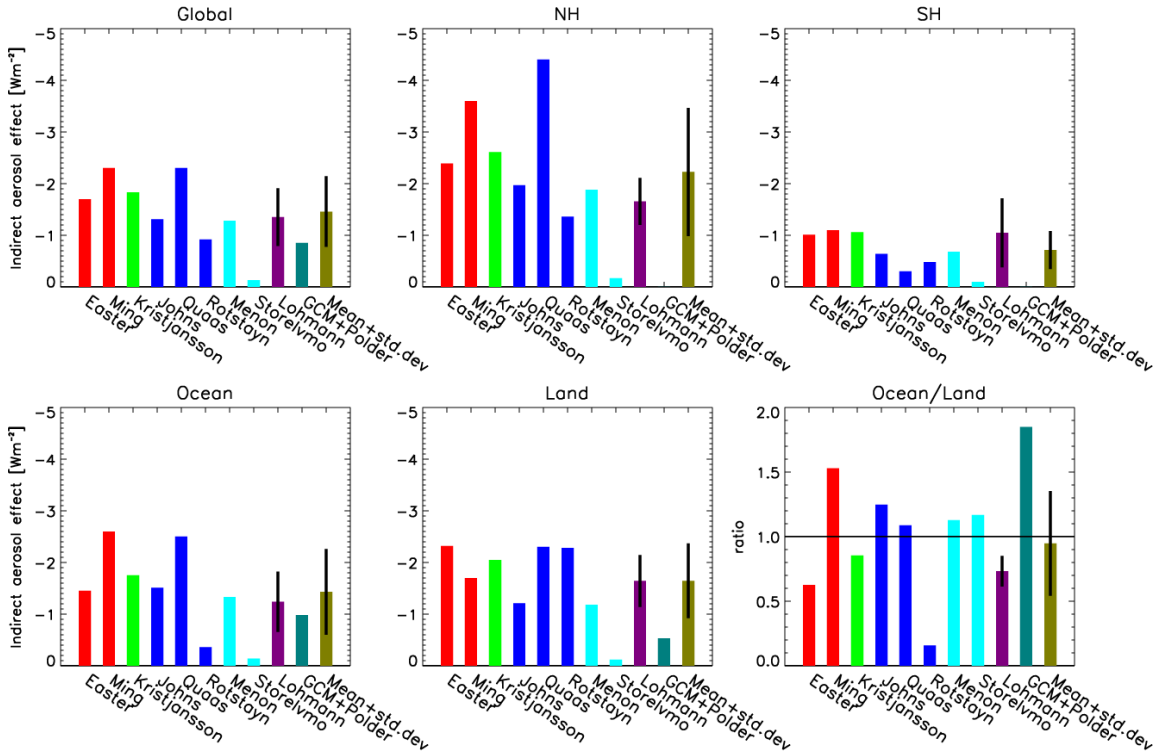

Figure 7.5.3. Global mean total anthropogenic aerosol effect (direct, semi-direct and indirect cloud albedo and lifetime effects) defined as the change in net radiation at the top-of-the-atmosphere from pre-industrial times to present-day and its contribution over the Northern Hemisphere (NH), Southern Hemisphere (SH), over oceans and over land, and the ratio over oceans/land. Red bars refer to anthropogenic sulphate (Easter et al., 2004; Ming et al., 2005[+]), green bars refer to anthropogenic sulphate and black carbon (Kristjánsson, 2002[*,+]), blue bars to anthropogenic sulphate and organic carbon (Johns et al., 2004[+]; Quaas et al., 2004[*,+]; Rotstayn and Liu, 2005[+]), turquoise bars to anthropogenic sulphate, black, and organic carbon (Menon and Del Genio, 2005; Storelvmo et al., 2005[*]), dark purple bars to the mean and standard deviations of anthropogenic sulphate, black, and organic carbon effects on water and ice clouds (Lohmann and Diehl, 2005), teal bars refer to a combination of ECHAM4 GCM and POLDER satellite results (Lohmann and Lesins, 2002) and olive bars to the mean plus standard deviation from all simulations.

[*] refers to estimates of the aerosol effect deduced from the shortwave radiative flux only
[+] refers to estimates solely from the indirect effects

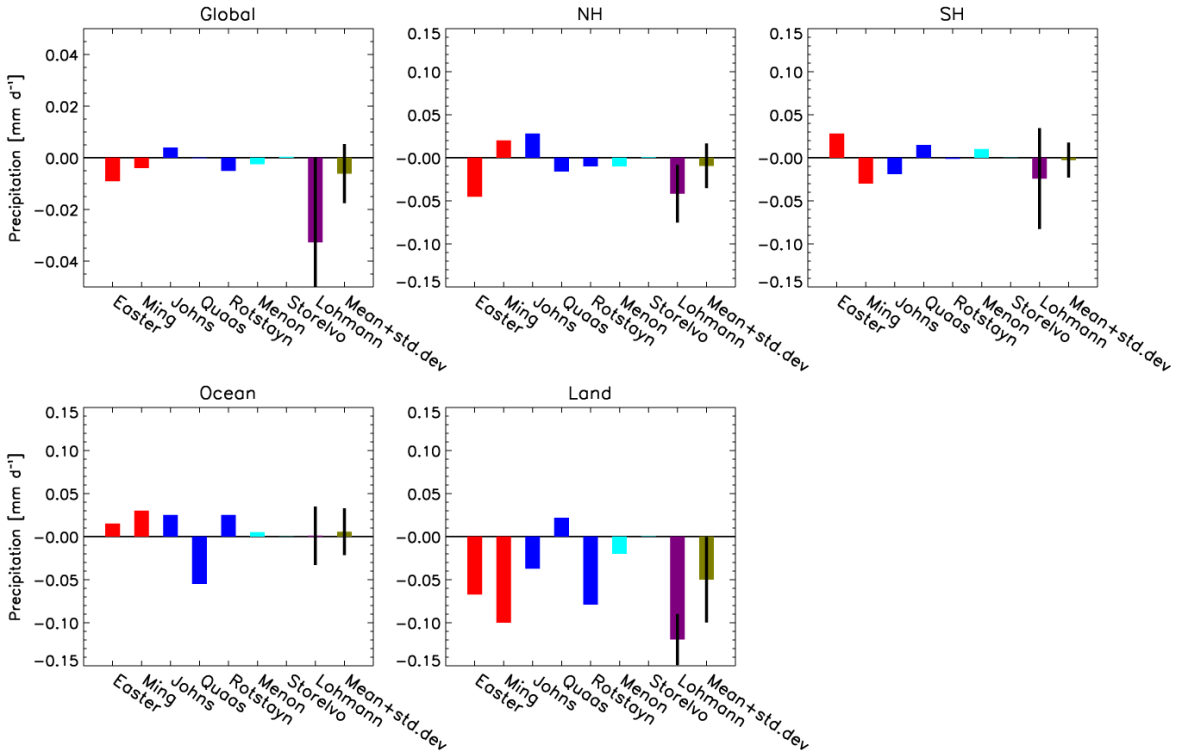

Figure 7.5.4. Same as Figure 7.5.3, but for precipitation. Note the different vertical scale for the global mean precipitation

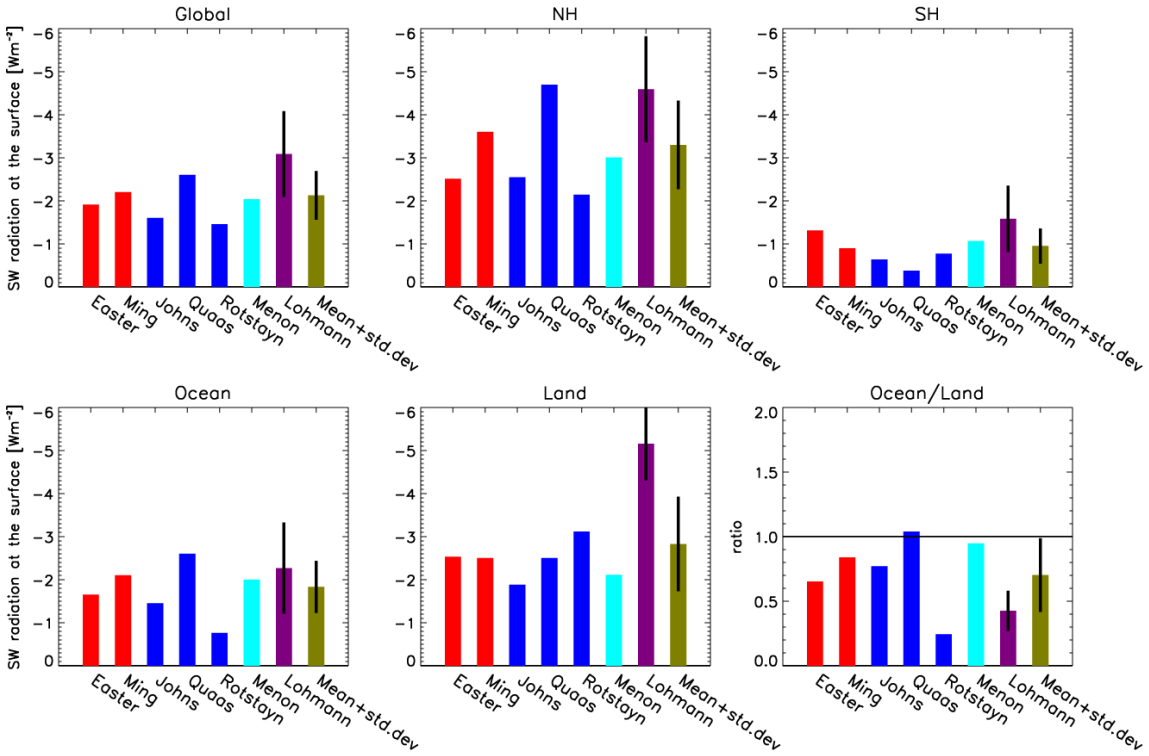

Figure 7.5.5. Same as Figure 7.5.3, but for the net shortwave radiation at the surface.

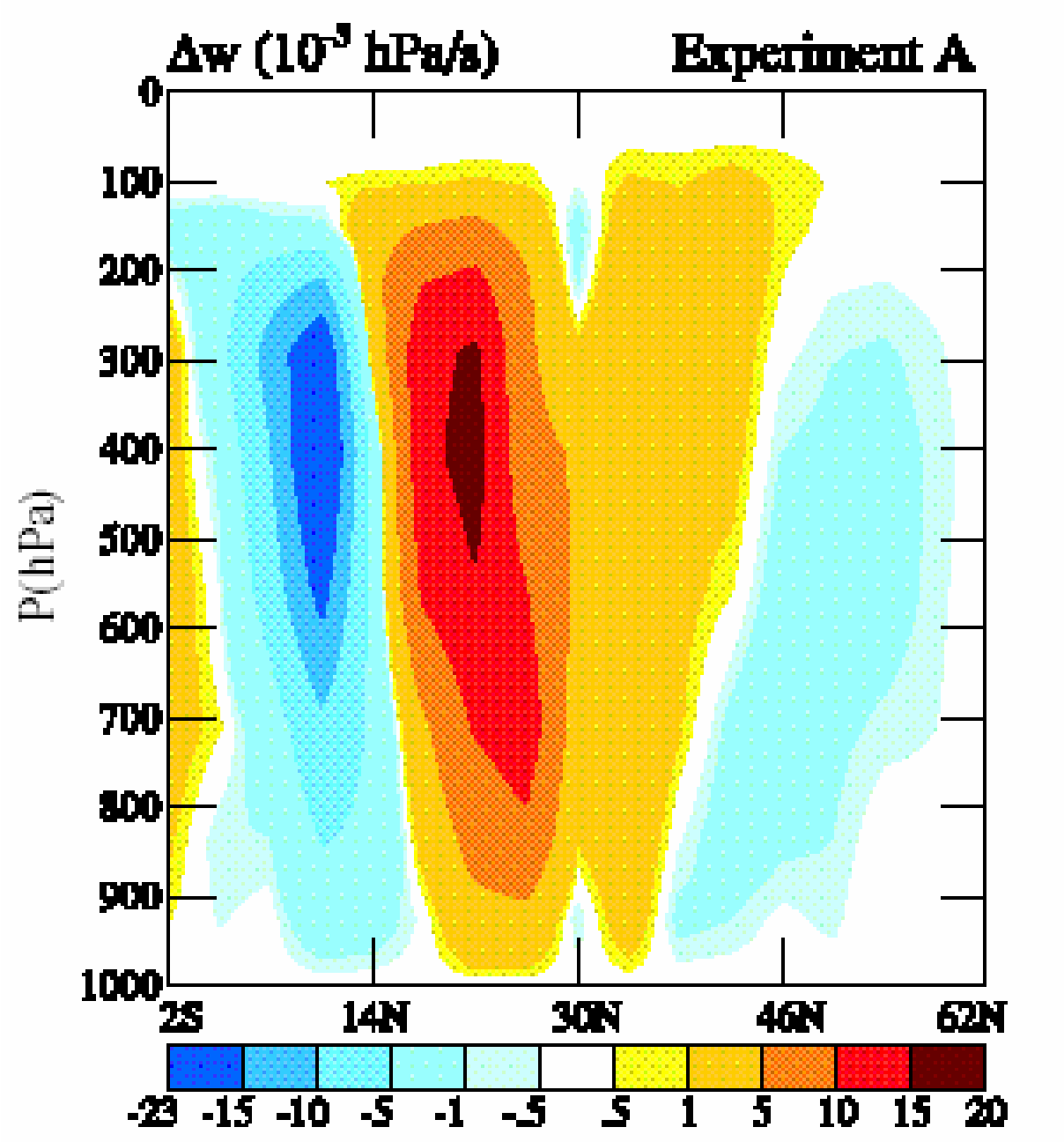

Figure 7.5.6. Simulated (GISS GCM) JJA vertical velocity change as a function latitude and altitude averaged over 90ºE to 130ºE for the experiment with aerosols representative of the measurements made over the Indian Ocean region and industrial regions of China (With courtesy from Menon et al., 2002b).

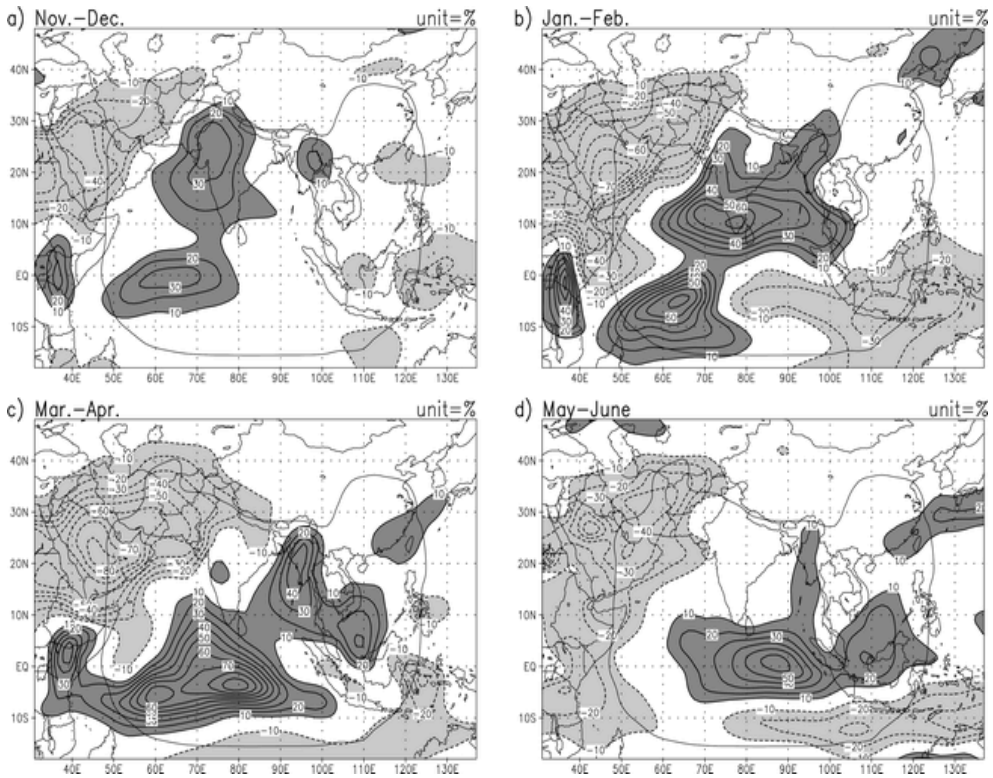

Figure 7.5.7. Percentage change in precipitation due to imposed aerosol forcing over the Indian Ocean region for a ratio of surface to atmospheric forcing of –0.9. The ellipse-like contour in the figure denotes the area where the forcing in the atmosphere exceeded 3 W m^{-2} (With courtesy from Chung et al., 2002).

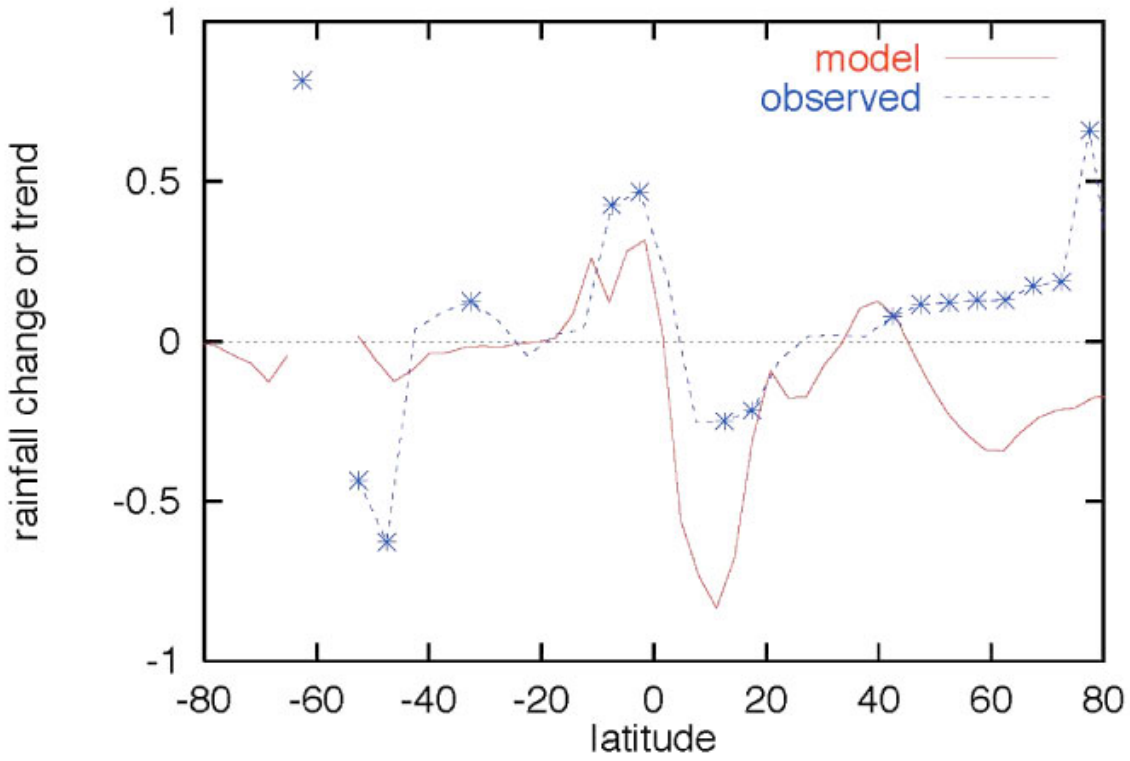

Figure 7.5.8. Zonally averaged trend in observed annual-mean precipitation over land for the period 1901–1998 after Hulme et al. (1998) in mm day^{-1} per century (blue dotted line) and zonally averaged difference in annual-mean precipitation over land between the present-day and pre-industrial simulations in mm day^{-1} (solid red line). Points at which the observed trend is (is not) significant at the 5% level are shown as asterisks (pluses). Courtesy of Rotstayn and Lohmann (2002).

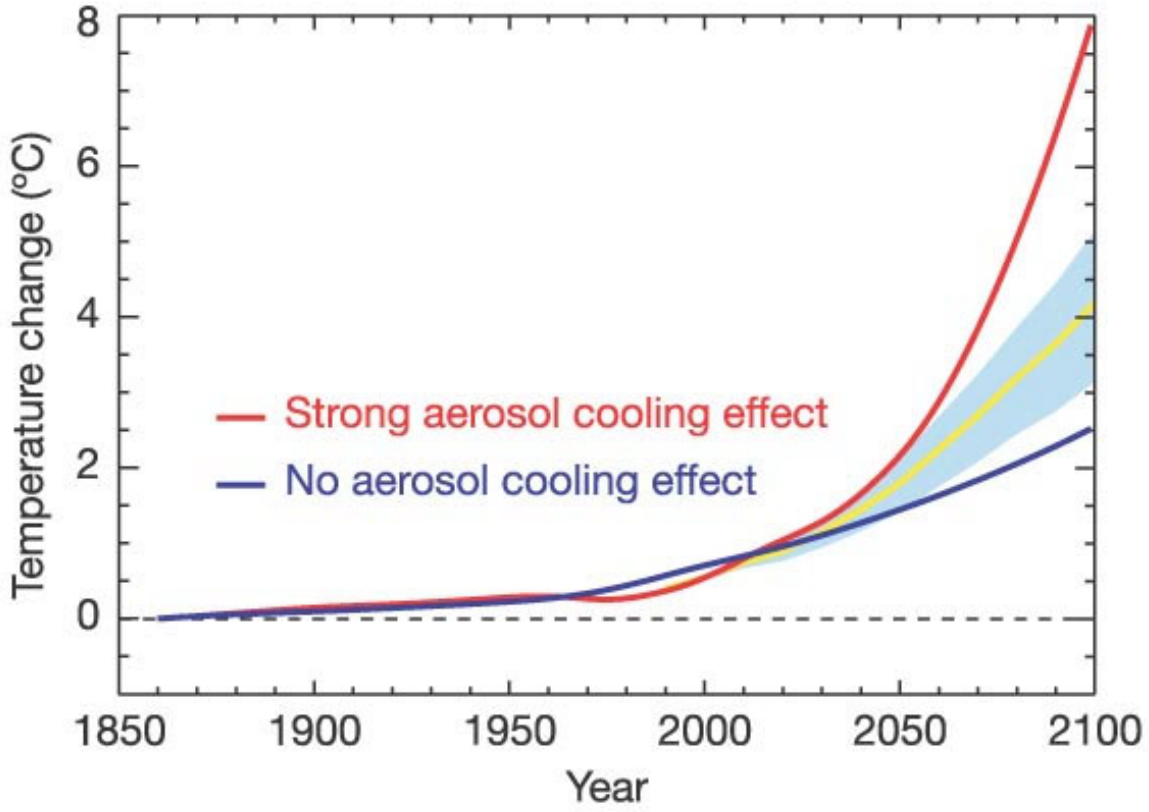

Figure 7.6.1. Temperature change simulated by Andreae et al. (2005) for the period 1850 to 2100.Two extreme cases are shown: strong present-day aerosol cooling consistent with 'forward' studies of aerosol effects on climate but with a climate sensitivity not ruled out by observations (red line, $Q_{aeros} = -1.7$ W m^{-2}), and the case of no aerosol cooling effect (blue line). The shading and the yellow line represent the range and central projection given in IPCC-TAR, based on the same scenario used in these calculations (scenario A2).

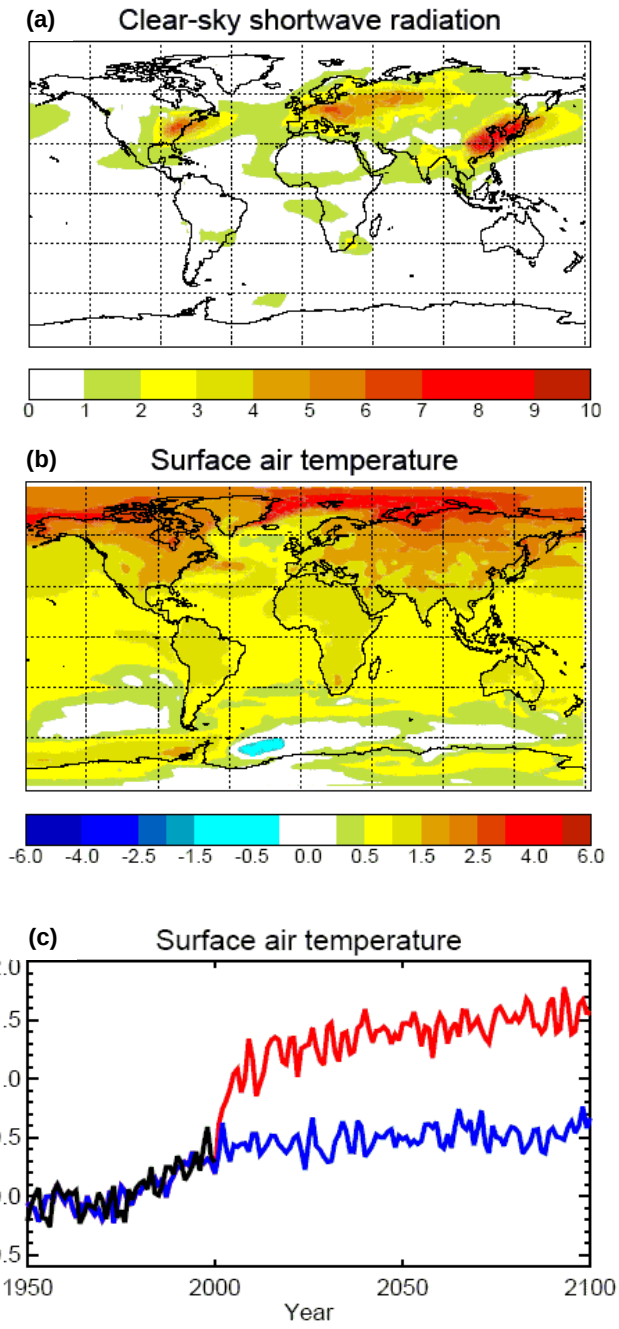

Figure 7.6.2. Effect of removing the entire burden of sulphate aerosols in year 2000 on (upper panel) the annual mean clear-sky top of the atmosphere shortwave radiation (W m^{-2}) calculated by Brasseur and Roeckner (2005) for the time period 2071–2100, and (middle panel) on the annual mean surface air temperature (°C) calculated for the same time period. Lower panel: temporal evolution of global and annual mean surface air temperature anomalies (°C) with respect to the mean 1961–1990 values. The evolution prior to year 2000 is driven by observed atmospheric concentrations of greenhouse gases and aerosols as adopted by IPCC (see Chapter 10). For years after 2000, the concentration of greenhouse gases remains constant while the aerosol burden is unchanged (blue line) or set to zero (red line). The black curve shows observations (Jones et al., 2001: Global and hemispheric temperature anomalies 1856–2000 – land and marine instrumental records. http://cdiac.ornl.gov/trends/temp/jonescru/jones.html).

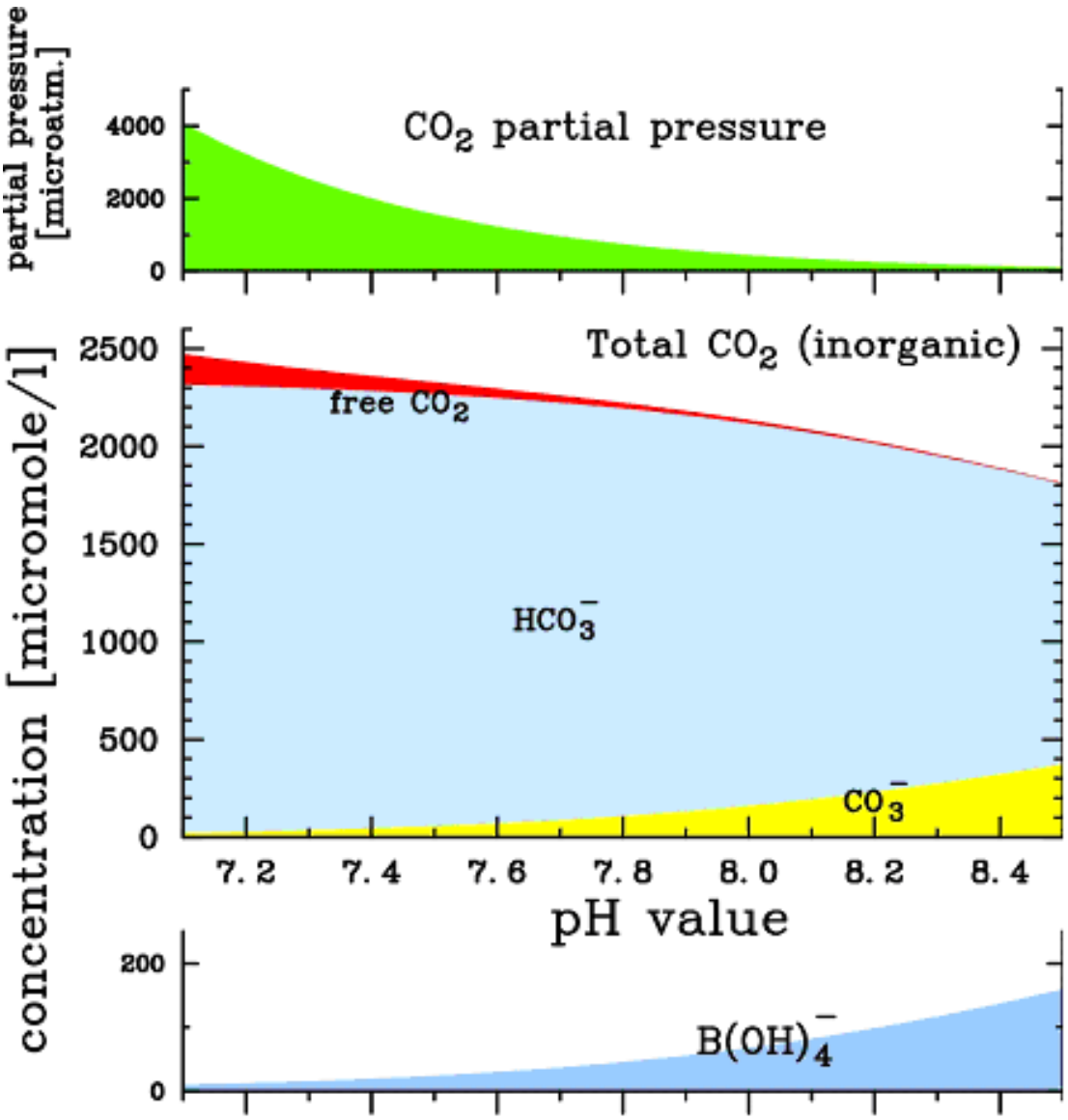

Box 7.1, Figure 1. The equilibrium partitioning of the different carbon species in seawater (at alkalinity 2350 µmol L^{-1}, temperature 15°C, salinity 35): A higher CO_2 partial pressure is directly coupled with a lower pH value, i.e., more acid conditions.

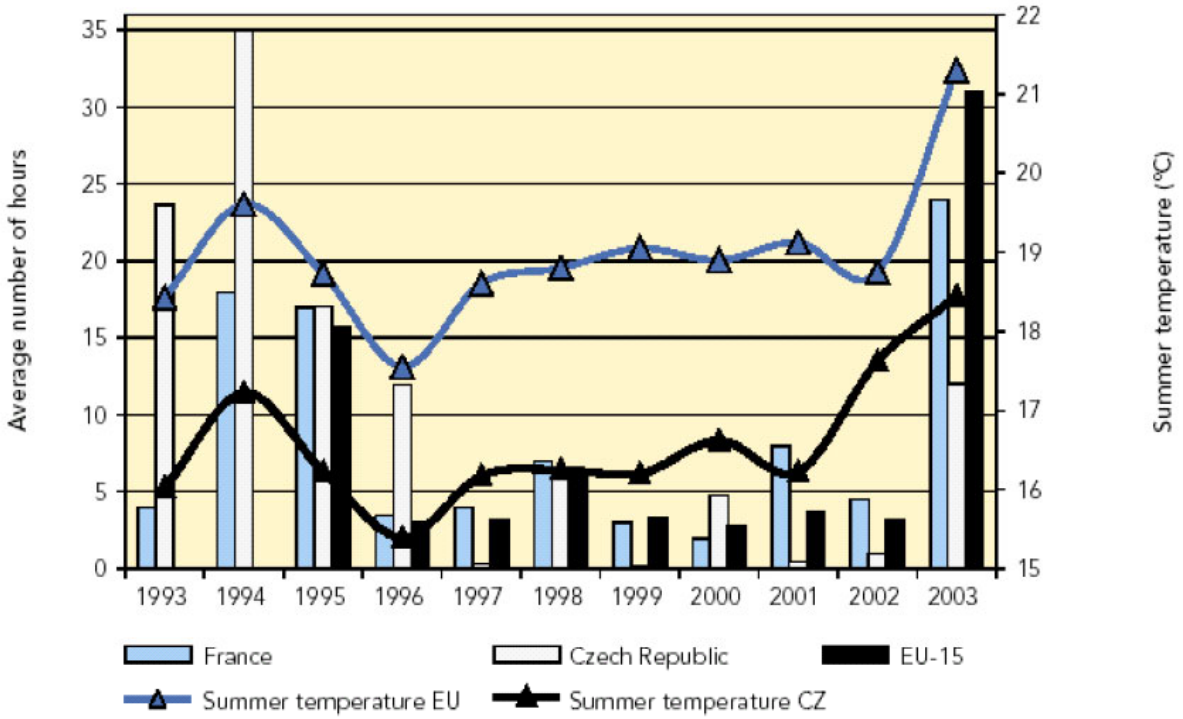

Box 7.2, Figure 1. Average number of hours with ozone concentrations exceeding 180 µg/m³ in France, the Czech Republic (CZ), and the European Union for the period 1993–2003, illustrating the strong link with temperature. From Science Panel on Atmospheric Research (2005).

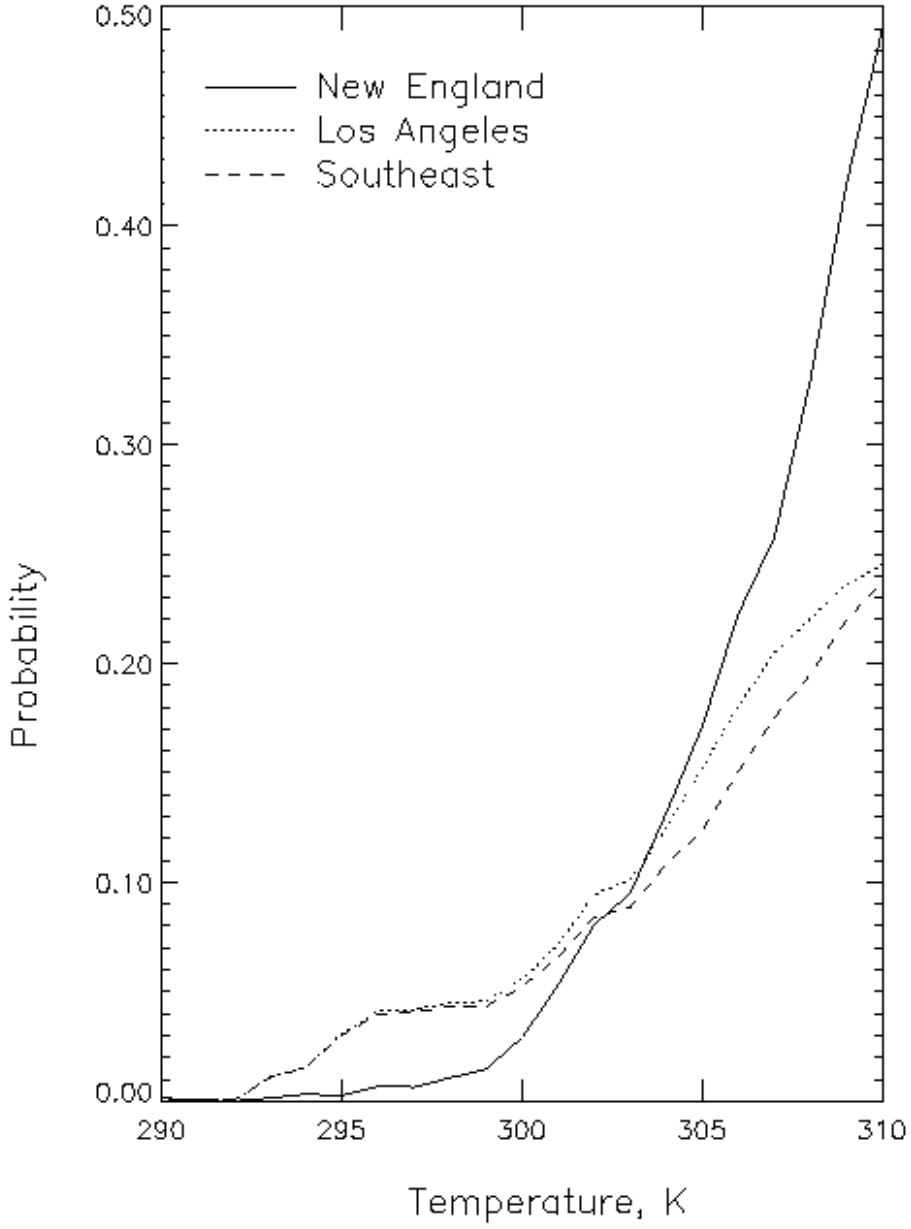

Box 7.2, Figure 2. Probability that the daily maximum 8-hour average ozone will exceed the U.S. National Ambient Air Quality Standard (NAQS) of 0.08 ppmv for a given daily maximum temperature, based on 1980-1998 data. Values are shown for New England (bounded by 36N, 44N, 67.5W, and 87.5W), the Los Angeles Basin (bounded by 32N, 40N, 112.5W, and 122.5W) and the southeastern United States (bounded by 32N, 36N, 72.5W, and 92.5W). From Lin et al. (2001).

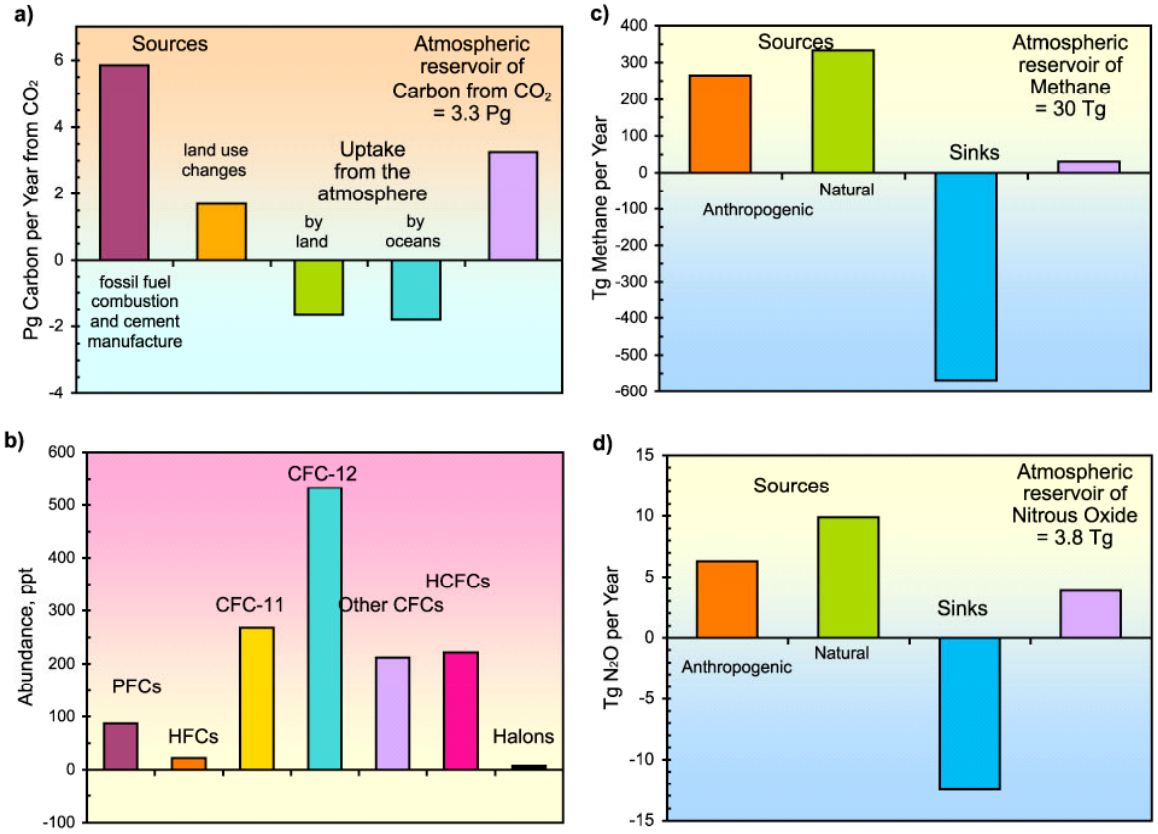

Question 7.1, Figure 1. Breakdown of contributions to the changes in atmospheric greenhouse-gas concentrations. (a) Human contributions to atmospheric carbon dioxide (CO_2) for 1980–2000. Each year carbon dioxide is released to the atmosphere by human activities including fossil fuel combustion and land use change. Not all of the carbon dioxide emitted remains in the atmosphere. Some is dissolved into the oceans and some is incorporated into plants as they grow. 1 Pg = 10^{15}g. (b) Atmospheric abundances in 1998 of CFCs and other halogen-containing compounds. These chemicals are exclusively human-produced. 1 ppt = 1 part in 10^{12}. (c) Sources and sinks of methane (CH_4). Anthropogenic or human-caused sources of methane include emission of methane from energy production, land fills, raising ruminant animals, rice agriculture and biomass burning. Tg = 10^{12}g. (d) As (c), but for nitrous oxide (N_2O). Anthropogenic or human-caused sources of N_2O include the transformation of fertilizer N into N_2O and its subsequent emission from agricultural soils, biomass burning, emissions from cattle and feedlots, and some industrial sources, including nylon manufacture.